JGR Solid Earth

RESEARCH ARTICLE
10.1029/2019JB018122

Key Points:
- A 3-D radially anisotropic model beneath Alaska is constructed by Bayesian Monte Carlo inversion
- The *V*sv part of the model captures many geological and tectonic features, including the Alaskan subduction zone and the cratonic roots
- The crustal radial anisotropy is strongest across areas that were subjected to significant extensional deformation in the Cretaceous

Correspondence to:
L. Feng,
lili.feng@colorado.edu

Citation:
Feng, L., & Ritzwoller, M. H. (2019). A 3-D shear velocity model of the crust and uppermost mantle beneath Alaska including apparent radial anisotropy. *Journal of Geophysical Research: Solid Earth*, *124*, 10,468–10,497. https://doi.org/10.1029/2019JB018122

Received 29 MAY 2019
Accepted 11 SEP 2019
Accepted article online 16 SEP 2019
Published online 25 OCT 2019

A 3-D Shear Velocity Model of the Crust and Uppermost Mantle Beneath Alaska Including Apparent Radial Anisotropy

Lili Feng[1] **and Michael H. Ritzwoller**[1]

[1]Department of Physics, University of Colorado Boulder, Boulder, CO, USA

Abstract This paper presents a model of the 3-D shear velocity structure of the crust and uppermost mantle beneath Alaska and its surroundings on a ~50-km grid, including crustal and mantle radial anisotropy, based on seismic data recorded at more than 500 broadband stations. The model derives from a Bayesian Monte Carlo inversion of Rayleigh wave group and phase speeds and Love wave phase speeds determined from ambient noise and earthquake data. Prominent features resolved in the model include the following: (1) Apparent crustal radial anisotropy is strongest across the parts of central and northern Alaska that were subjected to significant extension during the Cretaceous. This is consistent with crustal anisotropy being caused by deformationally aligned middle to lower crustal sheet silicates (micas) with shallowly dipping foliation planes beneath extensional domains. (2) Crustal thickness estimates are similar to those from receiver functions by Miller and Moresi (2018, https://doi.org/10.1785/0220180222). (3) Very thick lithosphere underlies Arctic-Alaska, with high shear wave speeds that extend at least to 120-km depth, which may challenge rotational transport models for the evolution of the region. (4) Subducting lithosphere beneath Alaska is resolved, including what we call the "Barren Islands slab anomaly," an "aseismic slab edge" north of the Denali Volcanic Gap, the "Wrangellia slab anomaly," and Yakutat lithosphere subducting seaward of the Wrangell volcanic field. (5) The geometry of the Alaskan subduction zone generally agrees with the slab model Alaska_3D 1.0 of Jadamec and Billen (2010, https://doi.org/10.1038/nature09053) except for the Yakutat "slab shoulder region," which is newly imaged in our model.

1. Introduction

Alaska is a region composed of crustal fragments squeezed between the Siberian and Laurentian cratons. It is characterized by a particularly variable crust that was built by subduction, large block rotation in the north (e.g., Moore & Box, 2016), extensional tectonics (e.g., Johnston, 2001; Plafker & Berg, 1994), and the successive accretion of terranes along both convergent and strike-slip fault systems in the south (e.g., Coney & Jones, 1985; Johnston, 2001). The active southern margin of Alaska is particularly complex, and tectonic growth is ongoing due to the underthrusting of the Pacific plate in the Alaska-Aleutian subduction zone and the collisional orogeny produced by the Yakutat crustal block as shown in Figure 1a, which is intersecting and subducting beneath at least parts of central Alaska (e.g., Haynie & Jadamec, 2017; Jadamec & Billen, 2010). The Yakutat microplate (Figure 1b, modified from Eberhart-Phillips et al., 2006) is the most recent exotic terrane assimilated onto the North American continent. All parts of Alaska continue to move relative to stable North America, and active seismicity is found across most of the state (Freymueller et al., 2008). The potential for damage caused by earthquakes, volcanic eruptions, and tsunamis is exceptionally high across a great deal of the state.

Interests in the geology, tectonics, and natural hazards of Alaska have motivated a rapid expansion of seismic instrumentation across the state, including the recently deployed EarthScope USArray Transportable Array (TA). These data now present an unprecedented opportunity to model the earth's crust and mantle beneath Alaska in a much greater detail.

Existing studies of the crust and mantle beneath Alaska have been based on a variety of types of data and approaches, including seismic refraction and reflection profiling (e.g., Fuis et al., 1995, 2008), receiver function analyses (e.g., Ferris et al., 2003; Miller et al., 2018; Miller & Moresi, 2018; O'Driscoll & Miller, 2015; Rondenay et al., 2010; Zhang et al., 2019), body wave tomography for isotropic and anisotropic structures (e.g., Eberhart-Phillips et al., 2006; Gou et al., 2019; Martin-Short et al., 2016; Tian & Zhao, 2012; Zhao et al., 1995), shear wave splitting studies (e.g., Christensen & Abers, 2010; Hanna & Long, 2012; Venereau

Table 1
Names of the Structural Features Identified with Abbreviations in Figure 1

Abbreviation	Name
AA	Arctic-Alaska
BA	Back-Arc
BR	Brooks Range
CC	Canadian Cordillera
CMF	Castle Mountain Fault
CM	Chugach Mountains
DF	Denali Fault
INFF	Iditarod-Nixon Fork Fault
KF	Kaltag Fault
NAC	North American Craton
NS	North Slope
TF	Tintina Fault
WT	Wrangellia Terrane
WVF	Wrangell Volcanic Field
YCT	Yukon Composite Terrane
YT	Yakutat Terrane

et al., 2019; Wiemer et al., 1999; Yang & Fischer, 1995), ambient noise tomography (e.g., Ward, 2015), and earthquake surface wave tomography (e.g., Wang & Tape, 2014). Some studies combined multiple data sets. For example, Allam et al. (2017) used body wave double-difference tomography and receiver functions to infer crustal and mantle structures along the Denali fault system. Ward and Lin (2018) performed a joint inversion of ambient noise surface waves and receiver functions to constrain shear wave speeds beneath Alaska. Jiang et al. (2018) used the ambient noise measurements from Ward and Lin (2018) and introduced longer period measurements from earthquakes and S-wave travel time residuals to construct an isotropic *V*s model of the crust and upper mantle. Similarly, Martin-Short et al. (2018) present results of a joint inversion of ambient noise, earthquake-based surface waves, P-S receiver functions, and teleseismic S-wave travel times.

The purpose of this study is to construct a 3-D model of apparent radial anisotropy of shear wave speeds (*V*sv and *V*sh) in the crust and upper mantle beneath Alaska using surface wave observations. The model is based on data recorded by the TA as well as other permanent and temporary networks in and around Alaska (Figure 1b). To achieve this purpose, we perform surface wave ambient noise tomography across Alaska as well as earthquake tomography, which extends dispersion measurements to longer periods. The resulting Rayleigh wave dispersion curves run from 8- to 85-s period and Love wave curves from 8- to 50-s period. The model may serve usefully as the basis for earthquake location and source characterization and to predict other types of geophysical data (e.g., body wave travel times, gravity, and perhaps mantle temperature). It may also serve as the basis for wavefield simulations (e.g., Feng & Ritzwoller, 2017), and radial anisotropy provides information about crustal and mantle deformation (e.g., Moschetti et al., 2010; Xie et al., 2013). It is also designed to provide a starting point for further studies that introduce complementary data sets (e.g., receiver functions, Rayleigh wave H/V ratio, Rayleigh wave azimuthal anisotropy, body waves, and shear wave splitting) to refine the model. Such refinements may result in better determination of shallower structures and internal interfaces within the Earth (e.g., Shen & Ritzwoller, 2016), as well as estimates of the full depth-dependent elastic tensor in the crust and mantle (e.g., Xie et al., 2015, 2017). Within a Bayesian Monte Carlo framework (e.g., Shen et al., 2013), we strive to provide reliable information about model uncertainties across the region of study, which will help guide the future use of the model.

The principal novelty of this study lies in the simultaneous interpretation of Rayleigh and Love wave data. By measuring dispersion curves from both types of surface waves, we are able to present the first model of *V*sh as well as *V*sv for the Alaskan crust and uppermost mantle. This results in the estimation of apparent radial anisotropy. There are three other noteworthy characteristics of the study. (1) We include data through February 2019, which improves data coverage, particularly for the Brooks Range and the Alaska North Slope, and the model extends over a larger region than many earlier studies. (2) By employing earthquake data, the resulting surface wave data set is broadband, extending from 8-s period up to 85-s period, which

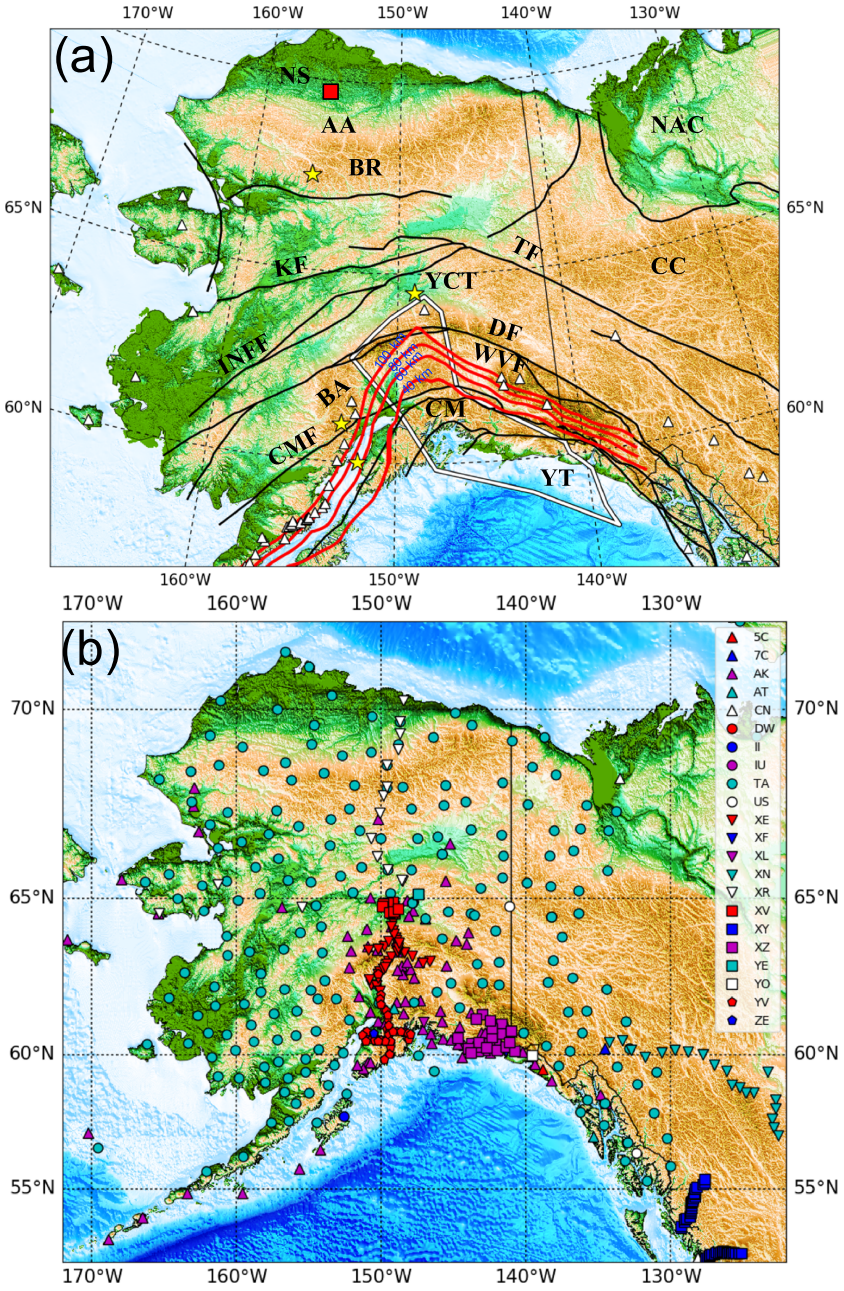

Figure 1. (a) Geologic and tectonic features and nomenclature. The black curves are major faults, and the four red curves are top edges of the subducting Alaskan-Aleutian slab at different depths. From south to north: 40, 60, 80, and 100 km (Jadamec & Billen, 2010). The white polygon is the hypothesized Yakutat Terrane (Eberhart-Phillips et al., 2006). Structural and tectonic features are identified with abbreviations explained in Table 1. The four yellow stars indicate sample grid points located in the Brooks Range (BR), the Aleutian slab Back-Arc region, the Cook Inlet, and the Yukon Composite Terrane (YCT) used in Figures 2, 6, 7, 8, 10, and 16, and the red square is the location in the Colville Basin used in Figure 7. (b) Station distribution. There are 22 networks indicated with different symbols. The USArray Transportable Array and the Alaska Network are the largest networks, identified with green circles and purple triangles, respectively.

allows simultaneous constraints to be placed on structures in the mantle and in the shallow crust. (3) We estimate model uncertainties, which guide the assessment and interpretation of the resulting 3-D model.

In discussing anisotropy using surface waves, it is useful to bear in mind two coordinate systems. The first is the frame defined by a symmetry axis (or foliation plane) of the medium of transport, in which "inherent" anisotropy is defined, and the second is the frame of the observations where "apparent" anisotropy is

Table 2
Description of Seismic Networks Used in This Study

Network	Description
5C	Dynamics of Lake-Calving Glaciers: Yakutat Glacier, Alaska
7C	The Mackenzie Mountains Transect: Active Deformation from Margin to Craton
AK	Alaska Regional Network
AT	National Tsunami Warning System
AV	Alaska Volcano Observatory
CN	Canadian National Seismograph Network
II	Global Seismograph Network (GSN - IRIS/IDA)
IU	Global Seismograph Network (GSN - IRIS/USGS)
PN	PEPP-Indiana
PO	Portable Observatories for Lithospheric Analysis and Research Investigating Seismicity
PP	Princeton Earth Physics Program
TA	USArray Transportable Array (NSF EarthScope Project)
US	United States National Seismic Network
XE	Broadband Experiment Across Alaskan Range
XN	Canadian Northwest Experiment
XR	Structure and Rotation of the Inner Core (ARCTIC)
XY	Batholith Broadband
XZ	STEEP: St. Elias Erosion and Tectonics Project
YE	Bench Glacier Seismic Network
YM	Denali Fault Aftershocks RAMP
YV	Multidisciplinary Observations of Subduction (MOOS)
ZE	Southern Alaska Lithosphere and Mantle Observation Network

defined. We follow Xie et al. (2017) and refer to measurements of anisotropy and inferences drawn from them in the observational frame as "apparent." Apparent S-wave radial anisotropy, also referred to as polarization anisotropy, is the difference in propagation speed between horizontally (*V*sh) and vertically polarized (*V*sv) S-waves, where *V*sh and *V*sv are properties of the medium defined in the observational frame. A common measure of the strength of apparent S-wave radial anisotropy is the Thomsen parameter (Thomsen, 1986; Xie et al., 2017), γ, which is approximated by

$$\gamma = \frac{V_{sh} - V_{sv}}{V_{sv}} \tag{1}$$

γ is inferred by simultaneously interpreting Rayleigh waves, which are dominantly sensitive to *V*sv, and Love waves, which are exclusively sensitive to *V*sh. Without introducing apparent radial anisotropy, Rayleigh and Love wave dispersion curves commonly cannot be fit simultaneously, a phenomenon often referred to as the "Rayleigh-Love discrepancy." Hereafter, whenever we refer to "radial anisotropy," we will mean apparent S-wave radial anisotropy.

Most studies of anisotropy, including this paper, report measurements and models of particular aspects of apparent anisotropy. In contrast, Xie et al. (2015, 2017) present methods that use observations of apparent radial and azimuthal anisotropy to infer characteristics of the depth-dependent elastic tensor, which possesses information about inherent anisotropy. In this study, we do not present azimuthal anisotropy; therefore, the inference of inherent anisotropy is beyond the scope of this paper.

Strong radial anisotropy (~4%) is a common mantle property (e.g., Ekstrom & Dziewonski, 1998; Kustowski et al., 2008; Marone et al., 2007; Montagner & Tanimoto, 1991; Nettles & Dziewoński, 2008; Shapiro & Ritzwoller, 2002; Yuan et al., 2011). This is often interpreted to result from the lattice preferred orientation of olivine, which is approximately an orthorhombic mineral, and develops due to strain caused by plate motions. In a number of regions around the earth (e.g., Tibet and western United States), strong crustal radial anisotropy has been found to coincide with extensional provinces (e.g., Moschetti et al., 2010; Xie et al., 2013), and this anisotropy is presumed to be caused by the lattice preferred orientation of crustal minerals, notably micas, whose foliation plane orients subhorizontally under significant horizontal strain. Thus, observations of apparent radial anisotropy provide qualitative information about the deformation state of the crust or upper mantle. In the long run, however, it may be worthwhile to consider observations of apparent radial anisotropy as a stepping stone to more complete estimates of the elastic tensor and inference of inherent anisotropy, as performed by Xie et al. (2015, 2017). In addition, we discuss radial anisotropy in

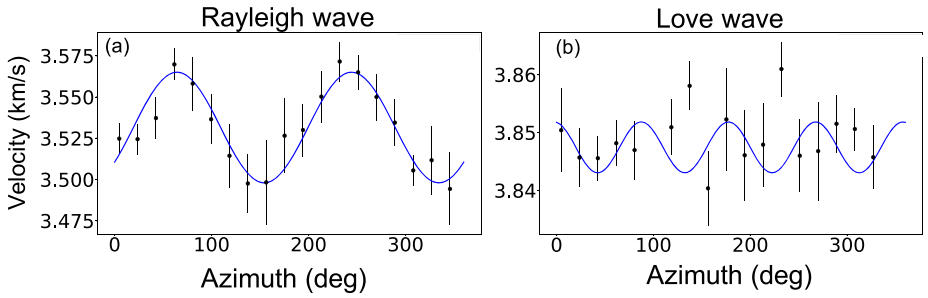

Figure 2. Azimuthal bin-averaged phase velocity measurements and bin standard deviations plotted versus azimuth (θ) measured using the eikonal tomography method in the Yukon Composite Terrane at 20-s period. (a) For Rayleigh waves, we fit a 2θ curve to the bin averages, where θ is azimuth. (b) For Love waves, we fit a 4θ curve. Interpretation of the azimuthal variation of the measurements is beyond the scope of this paper.

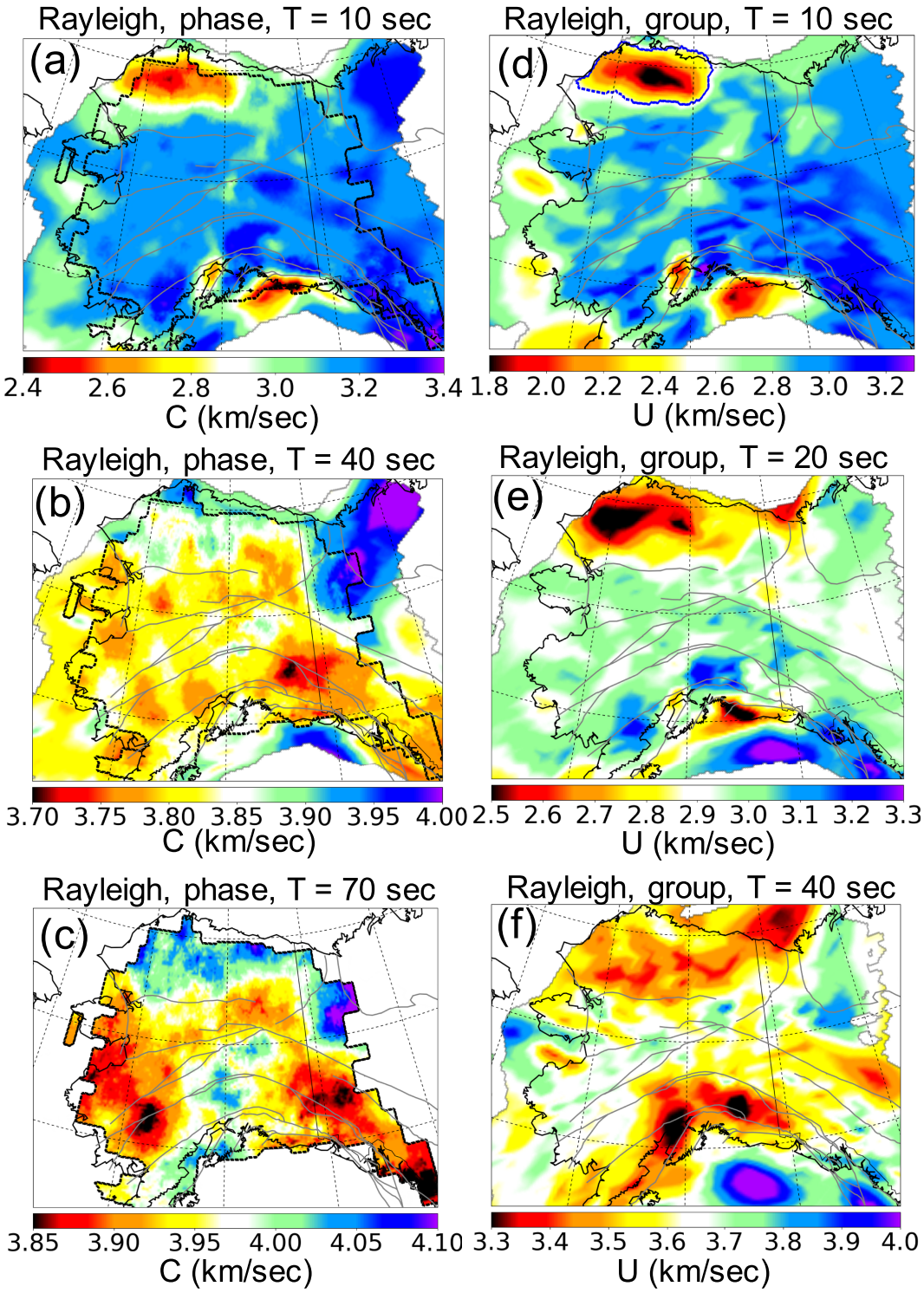

Figure 3. (a–c) Rayleigh wave phase speed maps at periods of 10 s, 40 s, and 70 s. The 10-s map is constructed from ambient noise tomography, 40-s map is from a combination of ambient noise and earthquake tomography, and the 70-s map is from earthquake tomography alone. (d–f) Rayleigh wave group speed maps for periods of 10, 20, and 40 s constructed with ambient noise tomography. The black piecewise linear contours in the left column enclose the regions where eikonal tomography is performed. Outside of these contours and for the maps in the right column, ray theoretic tomography is performed (Barmin et al., 2001). The dark blue dotted contour in (d) indicates the location of the North Slope foreland basin (Colville Basin), where the 10-s Rayleigh wave group speed is less than 2.5 km/s.

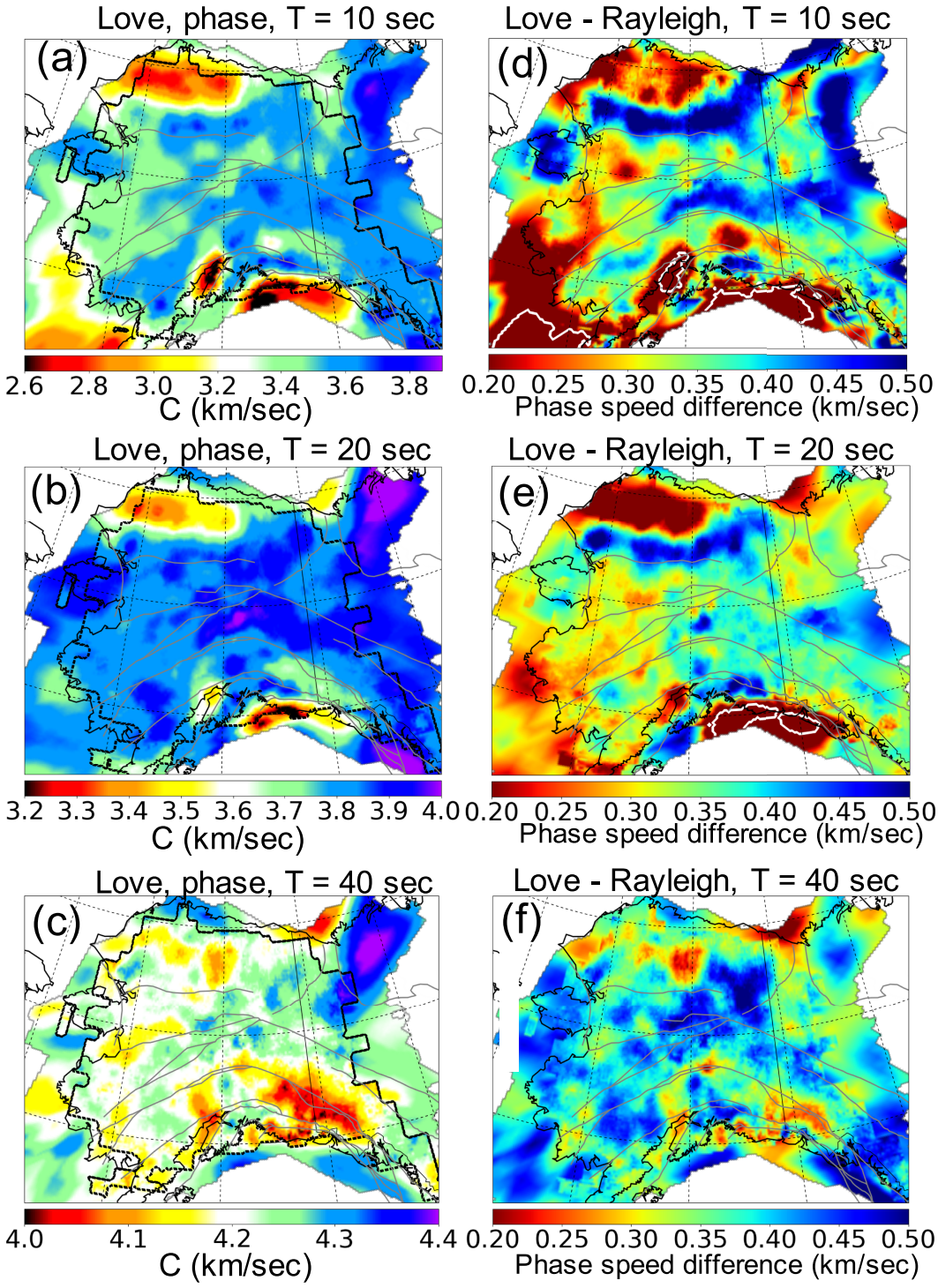

Figure 4. (a–c) Love wave phase speed maps at periods of 10, 20, and 40 s, where the 10 and 20 s maps are constructed using ambient noise tomography, and 40 s is from a combination of ambient noise tomography and earthquake tomography. (d–f) Differences in phase speed between Love waves and Rayleigh waves at 10, 20, and 40, respectively. The black piecewise linear contours in the left column enclose the regions where eikonal tomography is performed. Outside of these contours, ray theoretic tomography is performed (Barmin et al., 2001). The white contours in (d) and (e) are regions where the Love wave is slower than the Rayleigh wave, which occurs in wet regions.

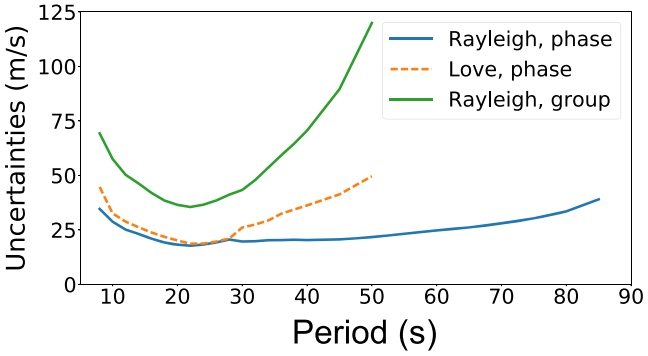

Figure 5. Estimated measurement uncertainties as a function of period averaged across the study region. The legend identifies the wave type for each curve. These uncertainties are twice the standard deviation of the mean of azimuthally binned standard deviations that result from eikonal tomography (e.g., Figure 2).

the North Slope foreland basin, or the Colville Basin (Bird & Molenaar, 1992), which is the largest basin in Alaska.

The paper is organized as follows. In section 2 we present information about the data sets and the tomographic methods used in this study, including how we estimate uncertainties. Section 3 presents the 2-D phase and group speed maps along with corresponding uncertainties, and section 4 shows how the shear wave speed model (*V*sv and *V*sh) is produced by a Bayesian Monte Carlo inversion given dispersion data and uncertainties extracted from the tomographic maps. We present the features revealed by the model in section 5 and discuss them in section 6.

2. Data, Tomographic Methods, and Uncertainty Estimation

2.1. Data

This study utilizes seismic records from 22 permanent and temporary networks deployed across Alaska and northwest Canada between January 2001 and February 2019 (Figure 1b). There are 537 seismic stations in total. Network names are listed in Table 2. Among those networks, the largest are the TA and the Alaska Regional Network (AK), which consist of 198 and 112 stations, respectively, and together compose nearly 60% of the stations used.

We perform ambient noise data processing by following the procedures described by Bensen et al. (2007), Lin et al. (2008), and Ritzwoller and Feng (2019). The Rayleigh wave is retrieved from the vertical-vertical (ZZ) component of the noise correlations while the Love wave is obtained from the transverse-transverse (TT) component. We then measure Rayleigh wave phase and group speeds between 8- and 60-s period and Love wave phase speed between 8- and 50-s period across the entire study region using automated frequency-time analysis. Additionally, we obtain broadband waveforms from teleseismic earthquakes with Ms > 5.0 (about 1,500 events), from which we obtain Rayleigh wave phase speed measurements from 30-

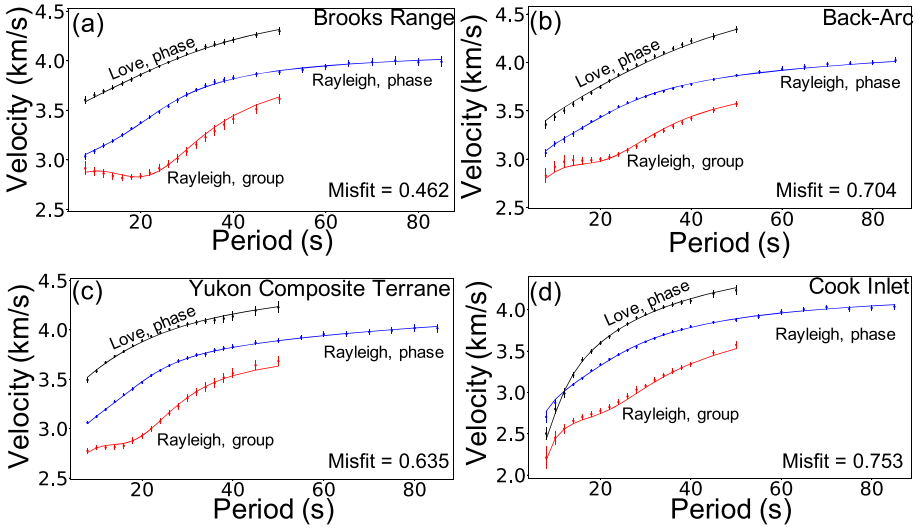

Figure 6. Examples of the Rayleigh wave phase and group speed curves and Love wave phase speed curves at four locations identified with yellow stars in Figure 1: (a) Brooks Range, (b) Aleutian Back-Arc, (c) Yukon Composite Terrane, and (d) Cook Inlet. The error bars (blue: Rayleigh wave phase, red: Rayleigh wave group, and black: Love wave phase) are observed dispersion measurements with one standard deviation uncertainty. Solid curves (blue: Rayleigh wave phase, red: Rayleigh wave group, and black: Love wave phase) are predictions from the 3-D model, namely, the mean of the posterior distribution of models at each depth including crustal and mantle anisotropy (*V*sv and *V*sh). Misfit is defined by equation (3).

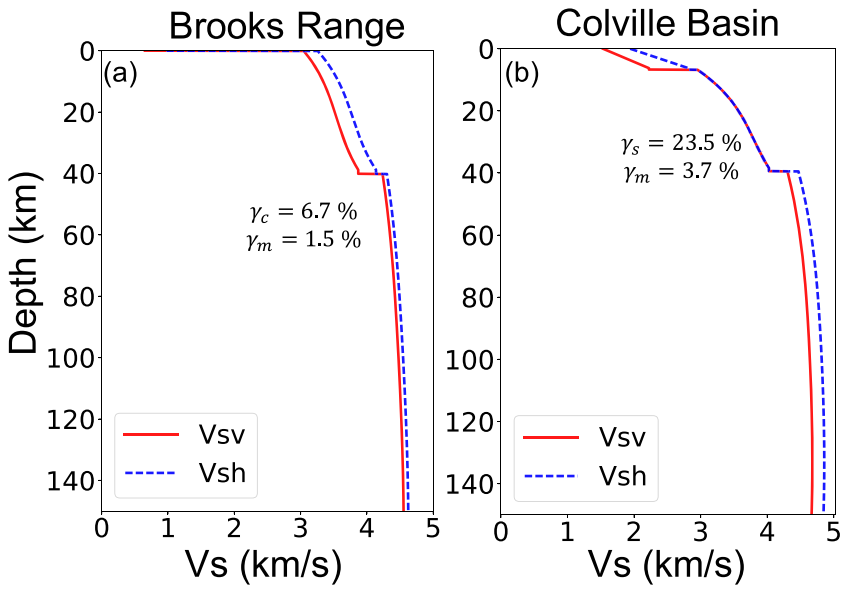

Figure 7. Examples of the mean of the posterior distribution plotted versus depth. (a) Brooks Range (yellow star in Figure 1a), *V*sv and *V*sh profiles with crustal and mantle anisotropy but no sedimentary anisotropy ($\gamma_s = 0, \gamma_c \neq 0 \neq \gamma_m$). (b) Colville Basin (red square in Figure 1a), *V*sv and *V*sh profiles with sedimentary anisotropy and mantle anisotropy but no crustal anisotropy ($\gamma_c = 0, \gamma_s \neq 0 \neq \gamma_m$).

to 85-s period and Love wave phase speed measurements from 30- to 50-s period to complement and augment the ambient noise data base.

2.2. Tomographic Methods

Where the distribution of stations is relatively dense and regular, we are able to perform eikonal tomography (Lin et al., 2009), a geometrical ray theoretical method, to produce phase speed maps from ambient noise dispersion data. Eikonal tomography results in local observations of phase speed and uncertainty versus the azimuth of propagation, as exemplified by Figure 2. For each grid point and period where eikonal tomography is performed, phase speed measurements are averaged in 18-degree azimuthal bins, and the standard deviation of the mean, σ_i, is computed for the measurements in each azimuthal bin i. The isotropic phase speed measurement for the grid point is the weighted average of the bin averages, where the weights are the reciprocals of the σ_i. The standard deviation of the isotropic phase speed is the mean of the bin standard deviations divided by the square root of the number of bins. Interpretation of the azimuthal variation of the measurements is beyond the scope of this paper.

The region where eikonal tomography has been applied is encircled with black dashed lines in Figures 3a–3c and 4a–4c for Rayleigh and Love wave phase speeds, respectively. Elsewhere, where eikonal tomography is inapplicable, we apply a great-circle (or straight ray) tomographic method (Barmin et al., 2001), which extends the region of coverage substantially. The straight ray method is applied across the entire region of study to construct the Rayleigh wave group speed maps (Figures 3d–3f). The group speed measurements help to improve constraints on the shallower parts of the earth structure. We do not use Love wave group speed data because of lower quality. We also apply eikonal tomography to Rayleigh and Love wave earthquake travel time measurements to extend phase speed maps to longer periods. For long period surface wave data, Helmholtz tomography (Lin & Ritzwoller, 2011) is applied by computing the amplitude Laplacian terms in order to correct for finite frequency effects. However, we find that finite frequency corrections are smaller than the uncertainties of the maps, on average. Thus, finite frequency effects for the region of

Table 3
Specification of the Prior Distribution of Models

Model parameters	Range
Sediment thickness	0-2 m_0 (km)
Crustal thickness	$m_0 \pm 0.5\ m_0$ (km)
*V*s, top of sediment	0.2-2 (km/sec)
*V*s, bottom of sediment	0.5-2.5 (km/sec)
B-spline coefficients, crust	$m_0 \pm 0.2\ m_0$ (km/sec)
Crustal anisotropy	±10%
B-spline coefficients, mantle	$m_0 \pm 0.2\ m_0$ (km/sec)
Mantle anisotropy	±10%

Note. m_0 is the reference value for each variable.

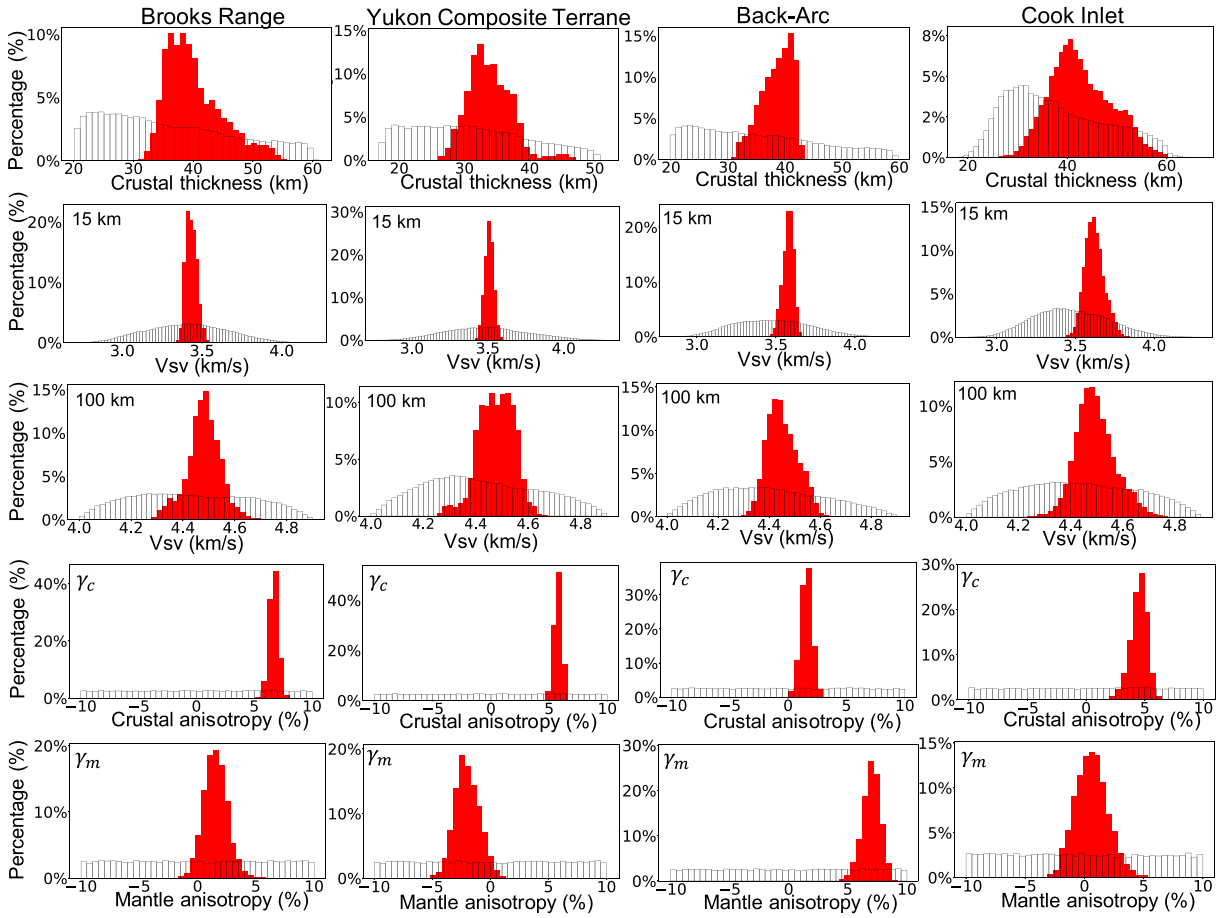

Figure 8. Examples of the prior and posterior marginal distributions for five model variables: crustal thickness, *V*sv at depths of 15 and 100 km, and crustal and mantle anisotropy (γ_c,γ_m) for the four locations identified with yellow stars in Figure 1 (Brooks Range, Yukon Composite Terrane, Aleutian Back-Arc, and Cook Inlet). The prior distributions are shown with white histograms whereas the red histograms indicate the posterior distributions.

study are not as strong as in the western United States (Lin & Ritzwoller, 2011). Consequently, we do not apply the finite frequency corrections in this study.

Comparisons of straight ray tomographic to eikonal tomographic maps have been presented by Lin et al. (2009) and Shen et al. (2016). There is typically a small mean difference caused by the fact that eikonal tomography models off-great circle propagation and maps constructed with that method are typically slightly slower than those based on great-circle rays. We see similar comparisons across Alaska. However, the two methods are consistent within the uncertainties of the maps, as long as the damping applied in the straight ray method is calibrated to match eikonal tomography in the region of overlap of the methods. Thus, straight ray tomography can be applied reliably to extend the coverage of the dispersion maps outside the zone of applicability of eikonal tomography.

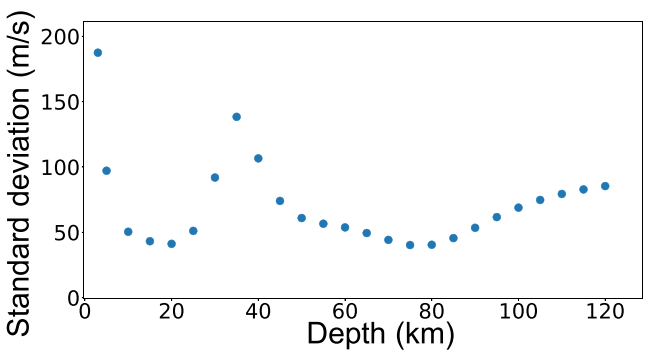

Figure 9. The standard deviation of the posterior distribution of *V*sv presented as a function of depth averaged over the region of study.

In practice, we construct the finalized phase speed maps by combining the ambient noise and earthquake measurements rather than performing tomography for each data set separately and then combining the dispersion maps. For Rayleigh waves, from 8 to 28 s, only ambient noise measurements are used, but from 30 to 60 s, the phase speed maps are constructed by averaging the ambient noise and earthquake measurements. Finally, for periods above 60 s, only earthquake measurements are used. For Love waves, from 8 to 28 s, only the ambient noise data set is used, but from 30 to 50 s, the phase speed maps are constructed using both ambient noise and earthquake measurements. The combination of

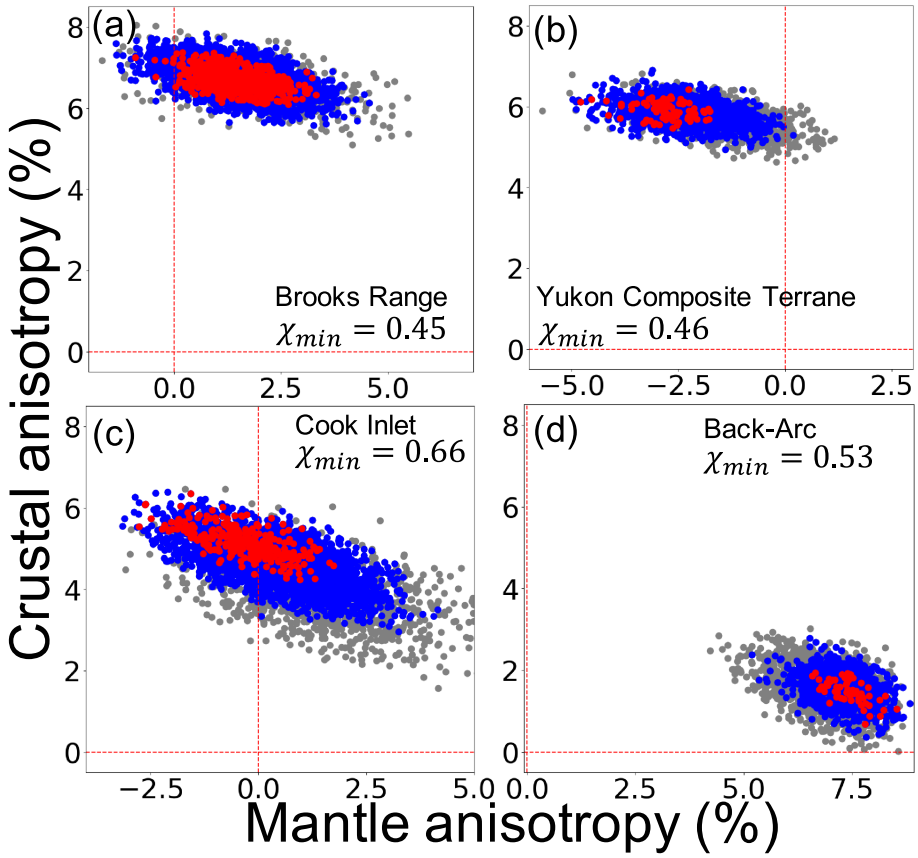

Figure 10. Trade-offs between crustal and mantle anisotropy (γ_c,γ_m) at the four locations identified with yellow stars in Figure 1: (a) Brooks Range, (b) Yukon Composite Terrane, (c) Cook Inlet, and (d) Aleutian Back-Arc. Symbol color indicates misfit χ from each of the accepted models, defined by equation (3). Red: $\chi < \chi_{min}+0.2$, blue: $\chi_{min}+0.2 \leq \chi < \chi_{min}+0.3$, and gray: $\chi_{min}+0.3 \leq \chi < \chi_{min}+0.5$, where χ_{min} is the misfit from the best fitting model at each location, which is labeled on each panel.

the two types of measurements (ambient noise and earthquake travel times) enhances the quality of the tomographic maps when both types of measurements are available and is motivated by the fact that the maps produced from ambient noise or earthquake data alone are consistent, as illustrated by Ritzwoller et al. (2011).

2.3. Uncertainty Estimates

As discussed in section 2.2, eikonal tomography produces uncertainty estimates where it is performed for phase speed. This approach does not estimate systematic errors or account for the correlation of errors in different travel time measurements. Therefore, as suggested by Lin et al. (2009), we multiply the error estimate from eikonal tomography by a factor of 2.0, which provides a more realistic estimate of uncertainty at each point on a phase speed map.

In the peripheral parts of the study region, where eikonal tomography cannot be performed, the maps derive from straight ray tomography (Barmin et al., 2001), which does not produce estimates of uncertainty but does provide resolution estimates. Similar to Shen et al. (2016), we infer uncertainties in these regions from resolution by applying an empirical scaling relationship that transforms resolution (in km) to uncertainty (in m/s) using the following formula:

$$\sigma(\boldsymbol{r}) = kR(\boldsymbol{r}) \tag{2}$$

where $\sigma(\boldsymbol{r})$ is the uncertainty estimate at location $\boldsymbol{r}$ where eikonal tomography has not been performed and $R(\boldsymbol{r})$ is the estimate of resolution, which is the standard deviation of the resolving kernel at the location

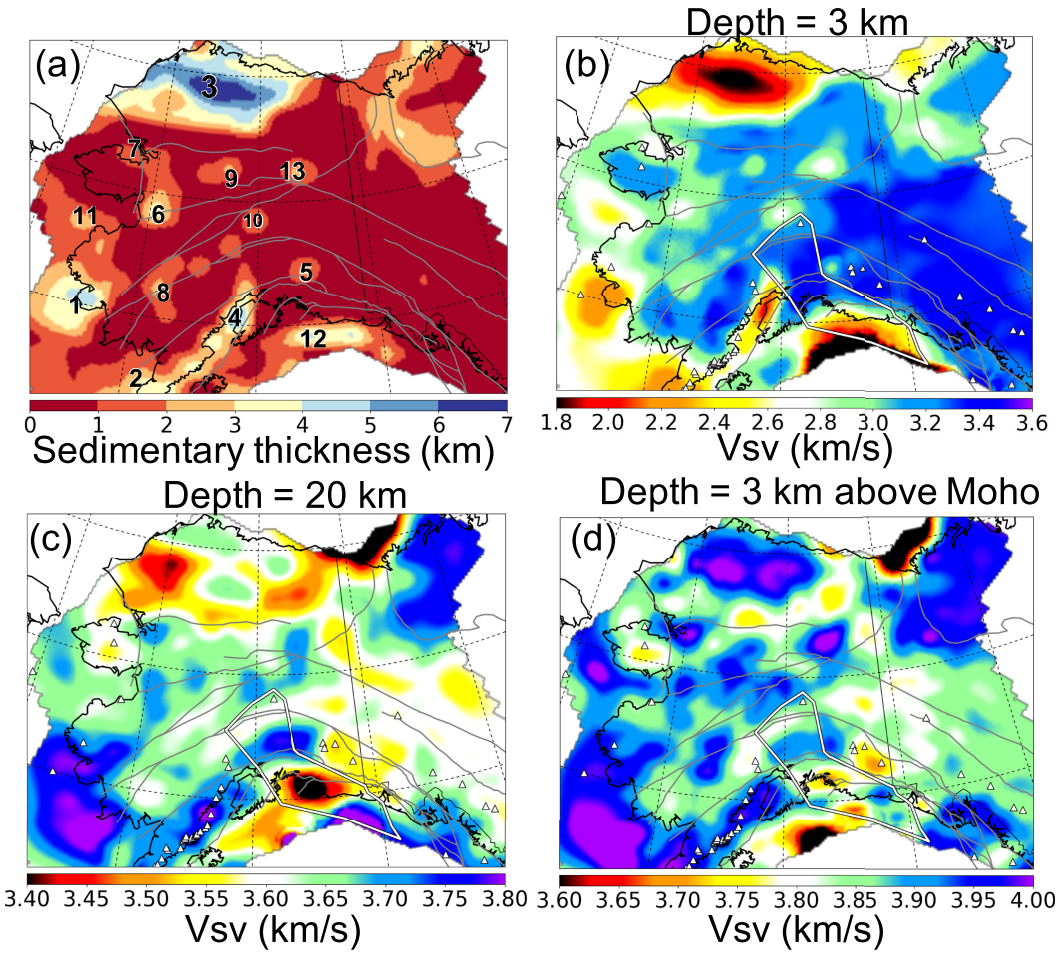

Figure 11. (a) Sedimentary thickness constructed with the mean of the posterior distribution of models, where the numbers and Table 4 identify basin names. (b–d) The mean of the posterior distribution of *V*sv for three depth ranges in the crust (central-depth ± 3 km) with central-depths of (b) 3 km, (c) 20 km, and (d) 3 km above Moho. Gray lines are major faults, the white polygon outlines the hypothesized Yakutat terrane, and triangles indicate volcanoes.

(Barmin et al., 2001). We estimate the value of k in equation (2) for each period separately at the grid points where both the eikonal and straight ray tomographic results are available. Typical values of k are ~0.2×10^{-3} s^{-1}, so that a 50-km resolution produces an uncertainty estimate of about 10 m/s.

Because we construct group speed maps with straight ray tomography, we must scale resolution to uncertainty everywhere. Uncertainties for group speed maps are also computed from equation (2), but we multiply k (determined for phase speed at that period) by a factor of 2.0, which amplifies group speed uncertainties by a factor consistent with relative data misfit found in constructing the dispersion maps. Absolute residuals for group speed measurements are typically about twice as large as phase speed residuals.

Spatially averaged uncertainties for Rayleigh and Love phase speeds, taken from the uncertainty maps, are shown in Figure 5. The spatial distribution of the uncertainties is quite homogeneous in the interior of the region of study but degrades in a systematic way near the periphery. Rayleigh and Love wave phase speed uncertainties average about 20–30 m/s but grow at the shorter and longer periods. Rayleigh wave group speed uncertainties tend to be about twice as large. The uncertainty in the difference between Love and Rayleigh wave speeds is about the square root of 2 times larger than uncertainties in either wave type. Love wave phase speed uncertainties grow to be larger than the Rayleigh wave uncertainties above 30-s period where earthquake data are introduced because earthquakes produce more high-quality phase time measurements for Rayleigh waves than for Love waves.

Table 4
Names of Sedimentary Basins Identified with Numbers in Figure 11a

Index	Name of the sedimentary basin
1	Bethel Basin
2	Bristol Bay Basin
3	Colville Basin
4	Cook Inlet Basin
5	Copper River Basin
6	Galena Basin
7	Hope Basin & Kotzbue Basin
8	Holtina Basin
9	Kobuk-Koyuku Basin
10	Nenana Basin
11	Norton Basin
12	Yakutat Basin
13	Yukon Flats Basin

3. Tomographic Maps

Examples of Rayleigh wave phase and group speed maps are presented in Figure 3. At 10-s period (Figures 3a and 3d), the Rayleigh wave is most sensitive to the uppermost crust including sedimentary basins. Several sedimentary basins, including the North Slope foreland basin, which we call the Colville basin, as well as several smaller basins are captured in the group speed map. Because group speed at each period has a shallower sensitivity than phase speed, the 20-s group speed map (Figure 3e) is qualitatively quite similar to the 10-s phase speed map (Figure 3a). The black contour on the 10-s group speed map (Figure 3d) identifies the Colville basin and is used later in the paper. The 40-s group speed (Figure 3f) strongly reflects changes in crustal thickness, where lower wave speeds indicate deeper crust. The high-velocity anomaly located in the northeast corner of the 40- and 70-s period Rayleigh wave phase speed maps (Figures 3b and 3c) identifies the North American craton. At 70 s, there are high-velocity anomalies associated with the subducting Pacific slab and the Arctic-Alaska craton.

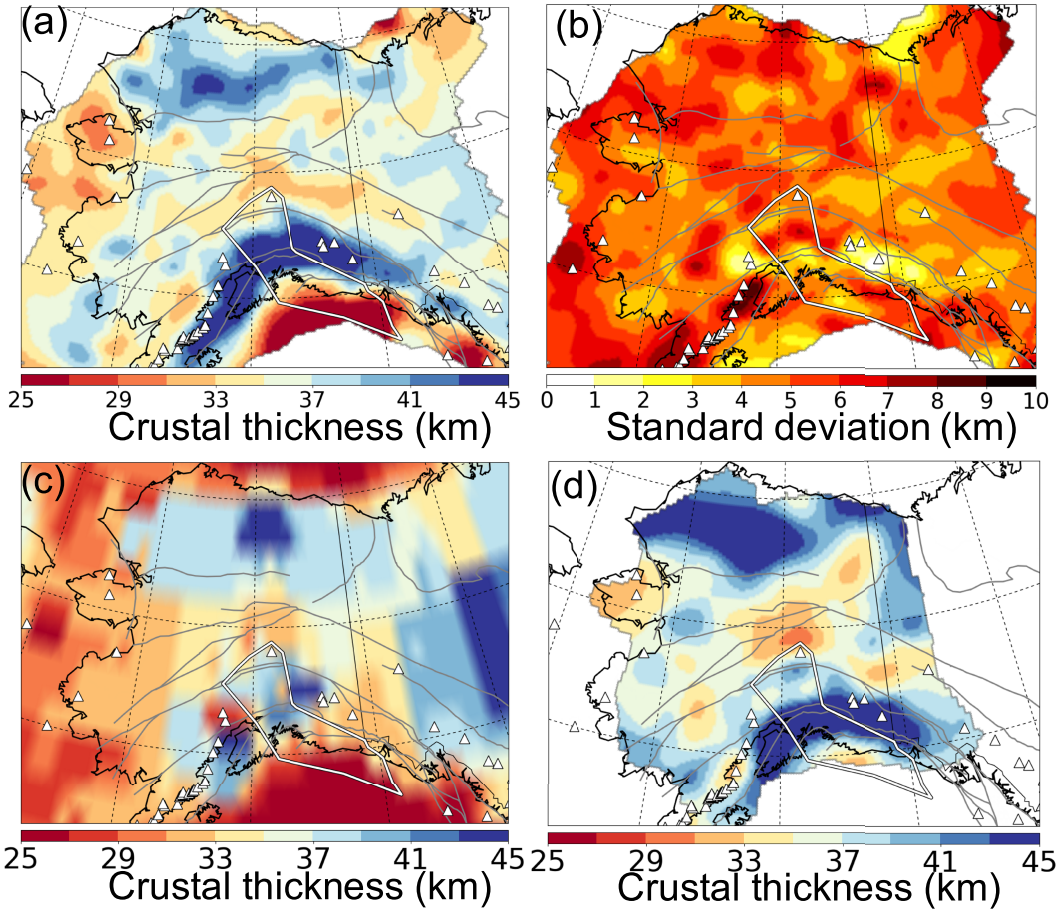

Figure 12. (a) Crustal thickness map constructed from the mean of the posterior distribution of models at each point. (b) Corresponding uncertainties of crustal thickness: standard deviation of the posterior distribution. (c) Crustal thickness from the Crust-1.0 model (Laske et al., 2013), which is part of the reference model used to define the prior distribution. (d) Crustal thickness estimated by Miller and Moresi (2018) using receiver functions, downloaded online (https://github.com/lmoresi/miller-moho-binder).

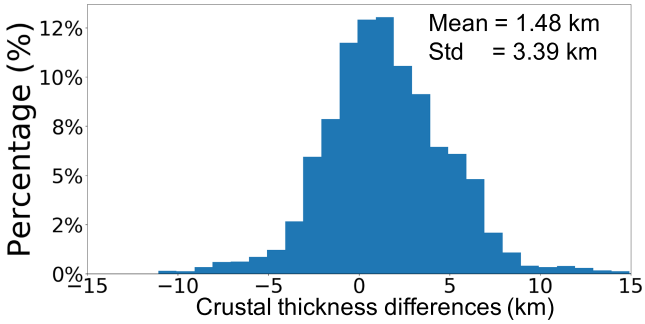

Figure 13. Histogram of differences in crustal thickness between our model and that of Miller and Moresi (2018), taken at grid points where both models exist. The mean difference and standard deviation of the differences are listed.

Figures 4a and 4c present examples of Love wave phase speed maps at periods of 10, 20, and 40 s. Love waves sample somewhat more shallowly than Rayleigh waves at the same period, so it is not surprising that the 20-s Love wave phase speed map is qualitatively similar to the Rayleigh wave map at 10-s period.

We also present the differences in phase speed between Love and Rayleigh waves in Figures 4d and 4f. The white contours identify the regions where the Love wave is slower than the Rayleigh wave, which is a consequence of the existence of a water layer and thick sediments. Fitting the difference between Rayleigh and Love wave velocities is one of the primary goals of a model of apparent radial anisotropy.

4. Constructing the 3-D Model

Local Rayleigh wave phase and group speed and Love phase speed curves with uncertainties are taken directly from the associated dispersion and uncertainty maps on a spatial grid with a 1.0° spacing in longitude and 0.5° spacing in latitude, resulting on average in about a 50-km grid spacing. Dispersion curves with uncertainties presented as error bars are shown for four example locations (Brooks Range, Yukon Composite Terrane, the Alaska subduction zone Back-Arc, and the Cook Inlet) in Alaska in Figure 6. These locations are identified with yellow stars in Figure 1a. Typically, Love wave phase speed is greater than Rayleigh wave phase speed at the same period, but there are exceptions in wet regions (oceanic sedimentary regions) at short periods (e.g., Cook Inlet, Figure 6d).

The local surface wave dispersion curves are the input for the Bayesian Monte Carlo inversion that produces a posterior distribution of vertical shear wave speed (*V*sv and *V*sh) profiles that predict the dispersion data acceptably. We closely follow the inversion procedure described by Shen et al. (2016), which consists of three steps.

(1) The first step is to construct the prior distribution of models on the 50-km grid. The grid spacing is chosen to be a bit smaller than the average station spacing in Alaska (~85 km). The prior distribution is controlled by the model parametrization, the reference model, and constraints on each model parameter. The range of the model variables is typically broad enough that an ensemble of models with acceptable data fits can be found.

(2) The second step is the Monte Carlo sampling of model space and determining data misfit. Based on the Metropolis algorithm (Mosegaard & Tarantola, 1995), we perform a series of random walks in model space

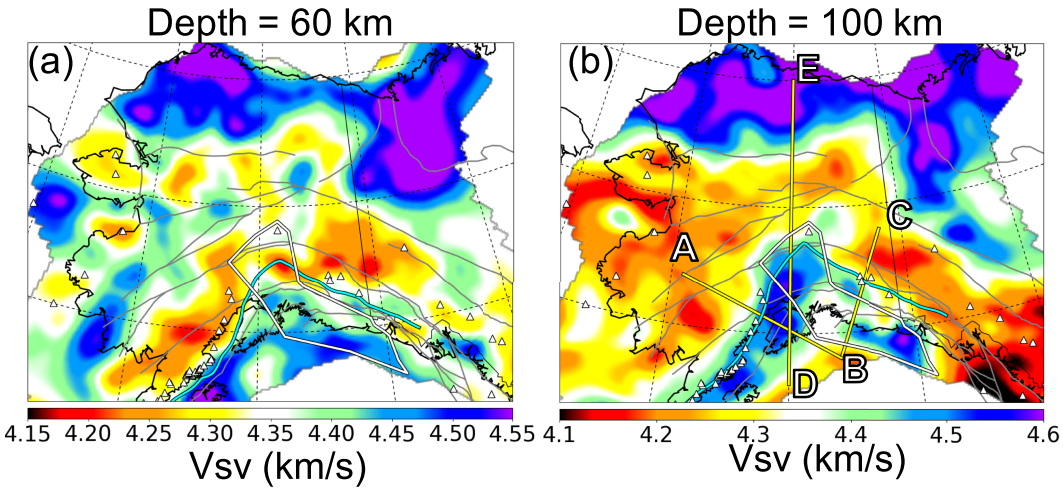

Figure 14. The mean of the posterior distribution of *V*sv models at two depth ranges in the mantle (central-depth ± 3 km) with central-depths of (a) 60 km and (b) 100 km. Symbols are similar to Figure 11, but additionally the cyan curve is the top edge of the subducting slab at each map depth from the slab model of Jadamec and Billen (2010) and the lines E-E′ identifies the vertical profile shown in Figure 21.

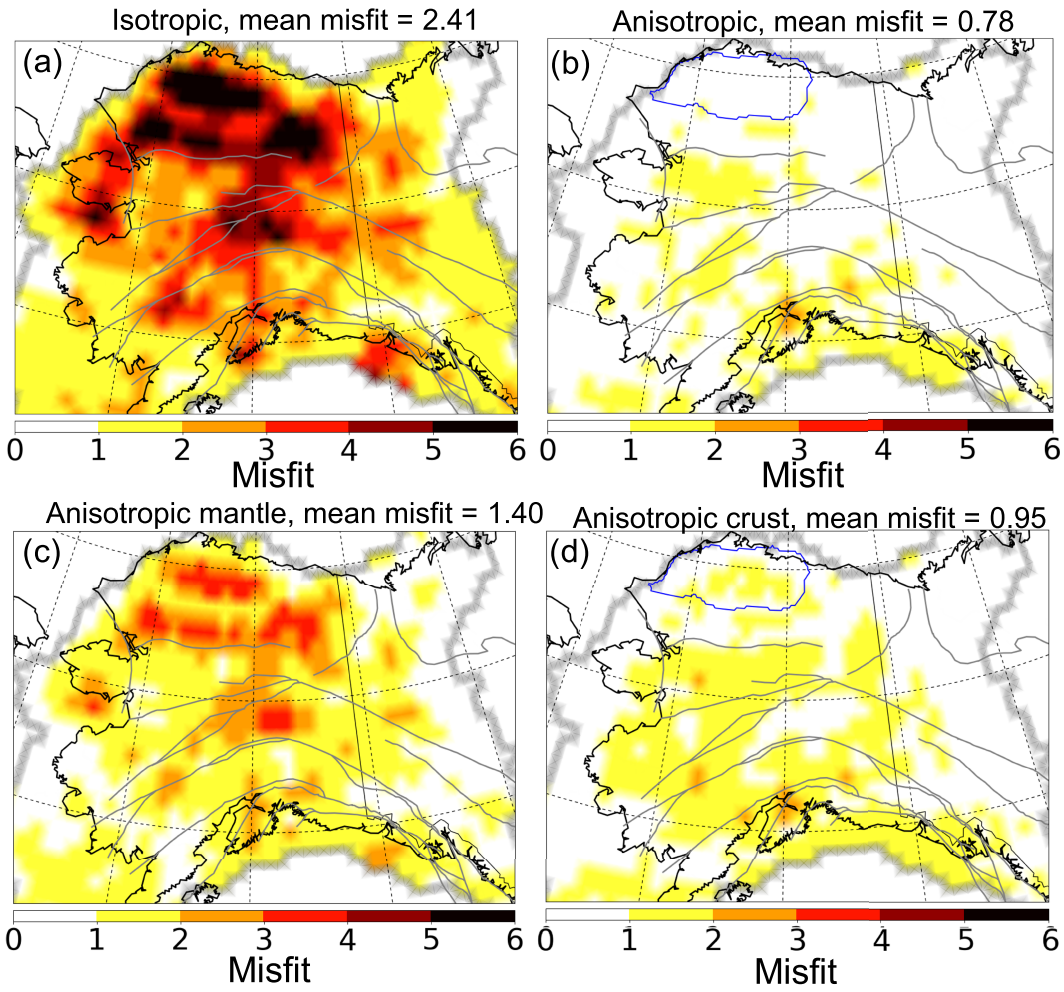

Figure 15. Misfit (defined by equation (3)) for the mean of posterior distribution of accepted models for different specifications of apparent radial anisotropy. (a) Isotropic model ($\gamma_s = \gamma_c = \gamma_m = 0$); inversion is performed using Rayleigh wave data alone. (b) Our final model based on both Rayleigh and Love wave data, including crustal and mantle anisotropy outside of the Colville Basin ($\gamma_s = 0, \gamma_c \neq 0 \neq \gamma_m$) and sedimentary and mantle anisotropy inside the Colville Basin ($\gamma_c = 0, \gamma_s \neq 0 \neq \gamma_m$). The Colville Basin is outlined in Figure 3d. (c) The model is based on both Rayleigh and Love wave data and includes mantle anisotropy but no sedimentary or crustal anisotropy ($\gamma_s = 0 = \gamma_c, \gamma_m \neq 0$). (d) The model is based on both Rayleigh and Love wave data and includes crustal or sedimentary anisotropy but no mantle crustal anisotropy ($\gamma_m = 0, \gamma_c \neq 0$ or $\gamma_s \neq 0$). The mean of the misfit across each map is labeled at the top of each panel.

that select a chain of candidate models in the prior distribution. For each individual model selected in the random walk, theoretical Rayleigh wave phase and group speed and Love wave phase speed curves are computed using the transversely isotropic forward code of Robert Herrmann's Computer Programs in Seismology (Herrmann, 2013) with earth flattening, and the misfit to the data at each point is calculated. Data misfit is defined as follows:

$$\chi = \sqrt{\frac{1}{N}\sum_{i=1}^{N}\frac{(d_i - p_i)^2}{\sigma_i^2}} \tag{3}$$

where d_i is an observed datum (Rayleigh wave phase or group speed or Love wave phase speed), p_i is the data value predicted from a given model, and σ_i is the one standard deviation data uncertainty. The index i ranges over dispersion data, where N is the number of the data values. A chain of candidate models terminates when sufficient steps have been taken to reach an equilibrium in model space and misfit. Then, the inversion starts afresh at a random point in the prior distribution with a new chain, and the procedure is repeated on the order of 300 times.

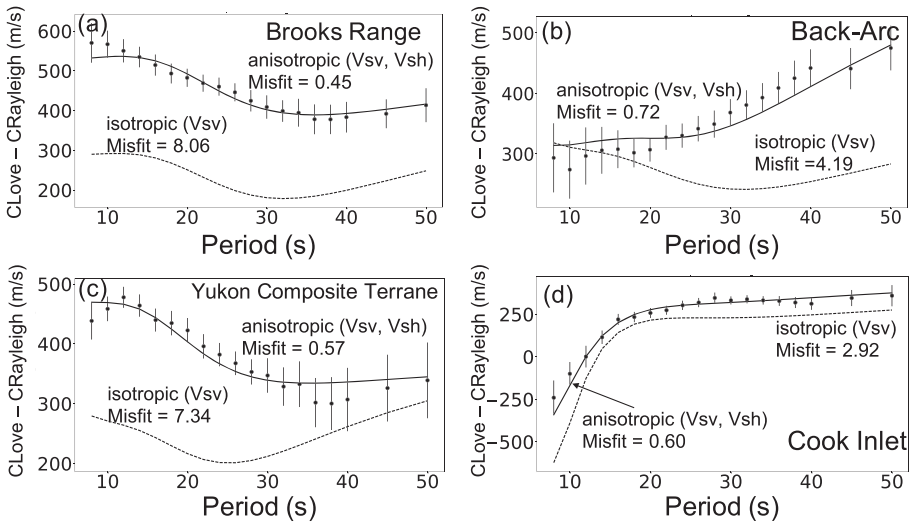

Figure 16. Examples of differences in phase speed between Love and Rayleigh waves at four locations identified with yellow stars in Figure 1: (a) Brooks Range, (b) Aleutian Back-Arc, (c) Yukon Composite Terrane, and (d) Cook Inlet. The error bars are standard deviation uncertainties of the differences between Love and Rayleigh wave phase speeds. The solid lines are the predictions from the mean of the posterior distribution of our final radially anisotropic model ($\gamma_m \neq 0, \gamma_s \neq 0$ or $\gamma_c \neq 0$), and the black dashed lines are from the isotropic *V*sv model ($\gamma_s = \gamma_c = \gamma_m = 0$). Misfit values from the isotropic and anisotropic models, defined by equation (3), are indicated on each panel.

(3) The third step is to construct the posterior distribution. After the second step terminates at each grid point, the model with the best data fit is identified as the "best fitting model" with misfit $\chi_{\min}$ and the "mean model" ($\overline{m}$) is defined as the mean of the ensemble of accepted models at each depth and for each discontinuity. Examples of average models at two locations are shown in Figure 7. A model is accepted if the misfit is less than $\chi_{\min}$+0.5, where $\chi_{\min}$ is the misfit value for the best fitting model.

4.1. Model Parametrization

The models we consider are essentially depth-dependent distributions of *V*sv and *V*sh, with *V*p and density scaled to *V*sv. *V*sh and *V*sv are related through equation (1), and we consider the shear wave speed part of the model specified by *V*sv and γ, where *V*sh = (1+γ)*V*sv. We set *V*ph = *V*pv and $\eta = 1$, which is physically unrealistic because *V*s anisotropy would be accompanied by *V*p anisotropy with $\eta \neq 1$ (e.g., Babuška & Cara, 1991; Erdman et al., 2013). However, as Xie et al. (2013) have shown, the effect of this assumption on estimates of *V*s radial anisotropy is negligible.

Each vertical profile on the ~50-km spatial grid across the study region consists of a vertical stratification of three categories of structure: the sediments, the crystalline crust, and the upper mantle. The first category is the sedimentary basin, which is represented by three model parameters: thickness and *V*sv at the top and bottom of the sediments. The *V*sv values in the sediments increase linearly from the top to the bottom. We assume that the sediments are isotropic, so that *V*sv = *V*sh, except in the Colville Basin where it is necessary to introduce nonzero sedimentary anisotropy, γ_s. The second category is the crystalline crust, which is described by thickness (from the base of the sediments to Moho), four cubic B-splines with variable coefficients, and the intensity of crustal radial anisotropy, γ_c, which is nonzero outside the Colville Basin. The third category is the mantle. *V*sv from the Moho to 200-km depth is determined with five cubic B-splines, while *V*sh is found from γ_m which is constant with depth. For offshore locations, an additional water layer is added to the top of the model, with water layer thickness determined from the ETOPO-1 model (Amante & Eakins, 2009) and *V*sv = *V*sh = 0 km/s, *V*p = 1.5 km/s, and density = 1.02 g/cm^3.

Once a *V*sv model is constructed for testing, *V*p is computed using *V*p/*V*sv = 2.0 in the sediments and *V*p/*V*sv = 1.75 in the crystalline crust and mantle. The density in the crust is determined from *V*sv and *V*p with the empirical relationship presented by Brocher (2005). In the mantle, however, density is scaled from *V*sv perturbations relative to 4.5 km/s with 10 kg/m^3 per 1% velocity change following Hacker and Abers (2004).

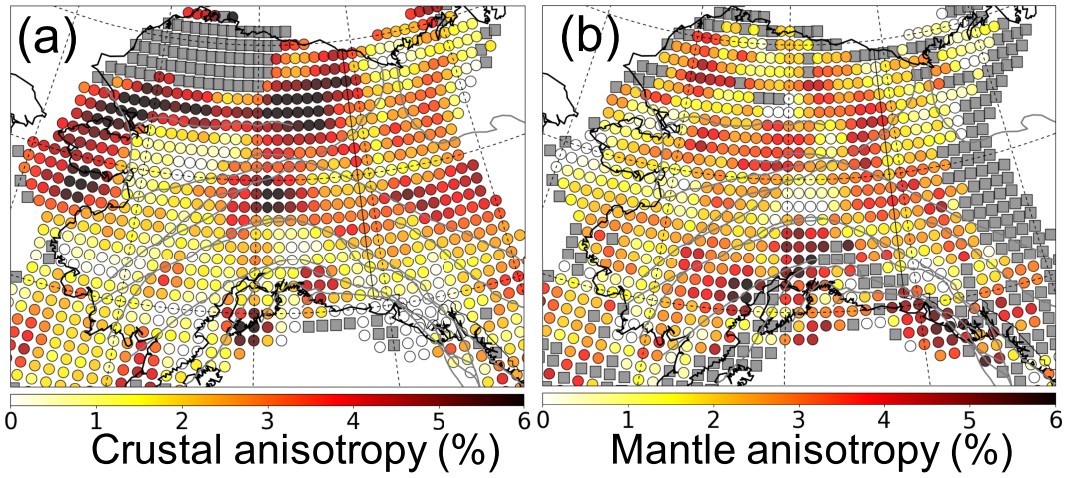

Figure 17. Apparent (a) crustal (γ_c) and (b) mantle (γ_m) radial anisotropy determined from the mean of the posterior distribution using both Rayleigh and Love wave data. We consider estimates of γ_c to be indeterminate if the standard deviation of the posterior distribution for γ_c is greater than 1.0% or in the Colville Basin where we estimate γ_s rather than γ_c. Estimates of γ_m are considered indeterminate if the standard deviation of the posterior distribution is greater than 1.5%. The gray squares identify the indeterminate grid nodes. This includes the whole of the Colville Basin for crustal anisotropy.

We assume that radial anisotropy is vertically constant and nonzero in the mantle, γ_m. In the crust, our parameterization of anisotropy depends on sedimentary thickness because in regions with very thick sediments, we are unable to estimate radial anisotropy reliably in the crystalline crust. The Colville Basin, identified by the dark blue contour in Figure 3d, is the region where the impact from the sediments on the estimation of crustal anisotropy is the most profound. Therefore, in the Colville Basin, we allow there to be sedimentary anisotropy but no crustal anisotropy ($\gamma_s \neq 0, \gamma_c = 0$) and consider crustal anisotropy to be indeterminate. In regions outside the Colville Basin, we set sedimentary anisotropy to zero but allow anisotropy in the crystalline crust ($\gamma_s = 0, \gamma_c \neq 0$).

The result is that the anisotropic part of the model is fully described by two different values of γ everywhere: one for the crust (γ_s or γ_c) and the other for the mantle (γ_m). As we show in section 5.2.1, this simple parameterization in which the amplitude of radial anisotropy is constant either in the sediments or in the crystalline crust and also in the upper mantle is sufficient to fit the data across the study region. However, this parameterization differs from the study of Xie et al. (2013), which found that substantial depth-variability of the strength of radial anisotropy was needed to fit the data in Tibet.

The shear Q values in the crust are fixed to the values in the ak135 model, namely, $Q = 80$ in the sediments and $Q = 600$ in the crystalline crust. With these values, there is little physical dispersion in the crustal shear modulus. Shear Q is fixed at 150 in the mantle for simplicity, which is similar to the choice by Shen and Ritzwoller (2016).

The resulting parameterization consists of 15 unknowns for each grid point: two for the sediments (Vsv), one for sediment thickness, four for the crystalline crust (Vsv), one for crustal thickness, five for the mantle (Vsv), and two for apparent radial anisotropy in order to find Vsh in the mantle and either the crystalline crust or sediments, that is, either (γ_c,γ_m) or (γ_s,γ_m).

4.2. Prior Distributions

The prior distribution used in the inversion involves variations around a reference model, which is a combination of the 1-D model ak135 (Kennett et al., 1995) with the 3-D CRUST-1.0 (Laske et al., 2013) model. The sedimentary and crustal thicknesses in the reference model are from CRUST-1.0, while the shear wave speeds in the crust and mantle are from ak135. The prior distribution defines a range of models around the reference model, where the range is determined from the parameterization of the model and the imposed constraints. The constraints we impose are of two types.

The first type of constraint is the allowed range of perturbations to the reference at each location, which prescribes the extent of model space explored in the Monte Carlo sampling. The allowed ranges on the 15

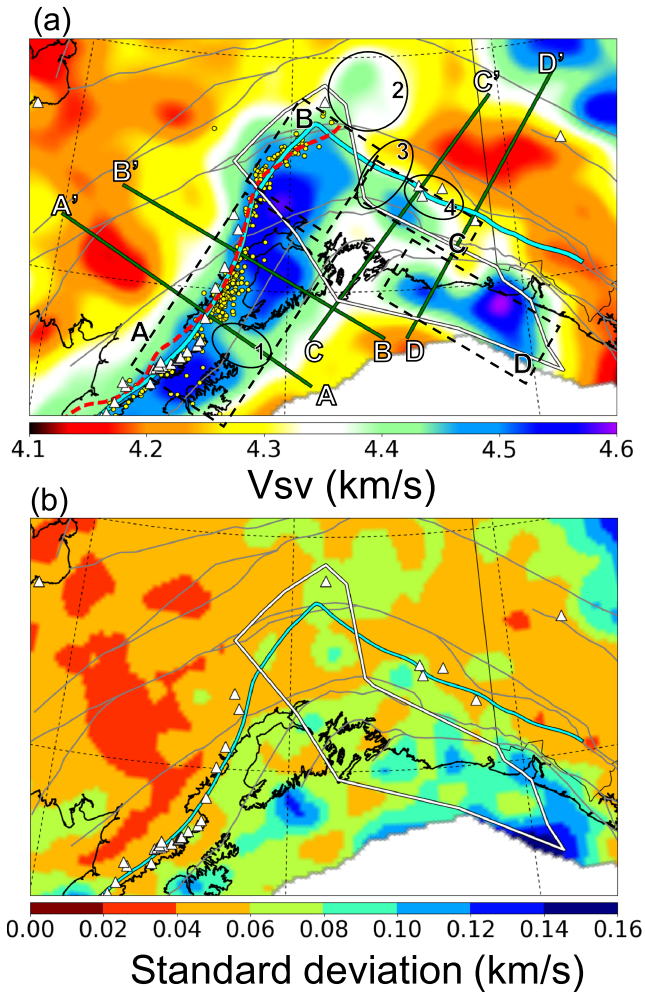

Figure 18. (a) Blow up of the *V*sv slice at 100 km with labels indicating different features of the subduction zone. Gray lines are major faults and the white contour outlines the hypothesized Yakutat Terrane. The cyan curve is the location of the edge of the subducting slab at 100-km depth from the slab model of Jadamec and Billen (2010), and the red dashed line delineates 100-km depth contour from the model Slab 1.0 (Hayes et al., 2012). The yellow dots indicate the locations of earthquakes from January 1991 to October 2015 (from ISC catalog) at depths from 95 to 105 km. Several tectonic features are identified with letters and numbers: A, Aleutian subduction zone; B, Alaskan subduction zone and slab kink which includes the Denali volcanic gap; C, Yakutat subduction zone; and D, Yakutat slab shoulder. The numbered ovals indicate the following: 1, the Barren Islands slab anomaly; 2, the aseismic slab edge; 3, the Wrangellia slab anomaly; and 4, the Wrangell volcanic field. Vertical profiles A-A′, B-B′, C-C′, and D-D′ are shown in Figure 19. (b) Corresponding uncertainty map of (a), indicating one standard deviation of the posterior distribution.

variables that define the 3-D model at each point are summarized in Table 3. For example, we allow there to be ±50% perturbations around the reference model for crustal thickness and ±20% for the B-spline coefficients in the crust and mantle. We also allow sedimentary thickness to vary from 0 to twice the input thickness from CRUST-1.0, and large changes to *V*sv in the sediments. Radial anisotropy in the crystalline crust, γ_c, and in the mantle, γ_m, range separately from ±10%, although beneath the Colville Basin $\gamma_c = 0$. Sedimentary anisotropy, γ_s, beneath the Colville Basin can range from 0% to 25% but is zero outside this basin. The result is that there are very large bounds considered around the reference model for the location of interfaces, shear wave speeds, and values for apparent radial anisotropy.

The second type of constraint involves explicit bounds imposed on aspects of each vertical model profile considered. There are eight prior constraints imposed in constructing candidate models allowed in the prior distribution. If a model profile is constructed that violates one of these constraints, it is rejected prior to computing data fit. (1) At jump discontinuities (base of the sediments, Moho), the jump is positive with

depth for both *V*sv and *V*sh. (2) Both *V*sv and *V*sh in the crust are less than 4.3 km/s at all depths. (3) Both *V*sv and *V*sh increase monotonically with depth in the crust, which we refer to this as the "monotonicity constraint." (4) At the top of the mantle, *V*sv and *V*sh are both less than 4.6 km/s and greater than 4.0 km/s. (5) At the bottom of the model, that is, at 200-km depth, *V*sv and *V*sh both are greater than 4.3 km/s. (6) Both *V*sv and *V*sh at all depths (0–200 km) are less than 4.9 km/s. (7) *V*sv and *V*sh are both greater than 4.0 km/s for depths below 80 km. (8) The difference at internal maxima and minima in *V*sv in the mantle is less than 10 m/s. Together these constraints act to discourage vertical oscillations in the crust and mantle, as well as large nonphysical excursions, and are hypotheses that we are testing. We should only infer a more complicated model if we cannot fit the data with these constraints in place. Despite this, some of the prior constraints are implemented due to limitation on what can be inferred from surface wave data. These constraints could be modified when other types of data are introduced that can constrain features that are not resolvable by surface wave data alone. For example, Brennan et al. (2011) reported the existence of a midcrustal discontinuity beneath the Alaska Range based on receiver functions. We do not allow a midcrustal discontinuity in this study. In the future, it would be natural to introduce receiver functions and modify the prior constraints in order to infer more detail about crustal structures. Receiver functions in Alaska, however, are often complicated and vary strongly with location (e.g., Miller & Moresi, 2018). This makes it challenging to implement single-station stacked or harmonic-stripped receiver function in a joint inversion with surface wave data for shear wave velocity structure, as performed by Shen and Ritzwoller (2016) for the lower 48 states. The multistation common Moho conversion point stacking method (e.g., Deng et al., 2015) may yield better receiver function information for the joint inversion procedure, which could provide more detail information about crustal structures.

Examples of prior distributions for several locations are shown with white histograms in Figure 8. The prior distributions of crustal and mantle radial anisotropy are nearly uniform, because there are no additional constraints applied to them. The prior distributions for crustal thickness have a slight preference for smaller values, due to the monotonicity constraint (which ensures larger values of *V*s deeper in the crust). The monotonicity constraint also tends to skew the prior distributions for *V*sv and *V*sh at 15 and 100 km.

4.3. Posterior Distributions

Posterior distributions of models are constructed based on data fit by the models chosen in the Monte Carlo sampling of model space and reflect how well model characteristics are constrained by the data. As discussed earlier, a model is accepted into the posterior distribution if its misfit χ is less than $\chi_{\min}+0.5$, where $\chi_{\min}$ is the misfit value for the best fitting model. The mean and standard deviation of the posterior distribution define the 3-D model (termed the mean model, $\overline{m}$) and the uncertainty estimates (σ_m). As argued by Shen and Ritzwoller (2016), σ_m is too large to provide a reasonable estimate of uncertainty but does reflect relative uncertainty, which is useful to assess how well shear wave speeds and topography on internal interfaces are constrained by the data set.

Figure 7 shows examples of the mean model at two locations: beneath the Brooks Range where crustal anisotropy is nonzero and beneath the Colville Basin where sedimentary anisotropy is nonzero. These profiles illustrate that the resulting models are smooth in the crust and mantle, are monotonically increasing in the crust, have positive jumps in both *V*sv and *V*sh at the two discontinuities, and have depth-variable apparent radial anisotropy which is, however, constant in the mantle and sediments or crystalline crust.

Examples of marginal posterior distributions for the same four grid locations shown for the prior distributions are presented with the red histograms in Figure 8. These posterior distributions reveal that *V*sv in the interior of the crust and mantle are relatively well constrained. In contrast, near the boundaries of the crust the posterior distribution widens. This is illustrated in Figure 9, which shows the standard deviation of the posterior distribution averaged over the study region as a function of depth. In the interior of the crust and in the mantle between depths of about 50 and 100 km, the standard deviation of the posterior distribution is about 50 m/s. Near the boundaries in the crust the value more than doubles, and then it grows slowly at depths greater than 100 km. For this reason, we truncate the model and discuss its properties only to a depth of 120 km. Figure 8 also shows that the posterior marginal distribution for crustal thickness is quite wide. Indeed, with surface wave data alone, internal interfaces in the Earth are typically poorly determined (e.g., Shen et al., 2016). The posterior distributions also indicate that crustal radial anisotropy, γ_c, tends to be better constrained than mantle radial anisotropy, γ_m.

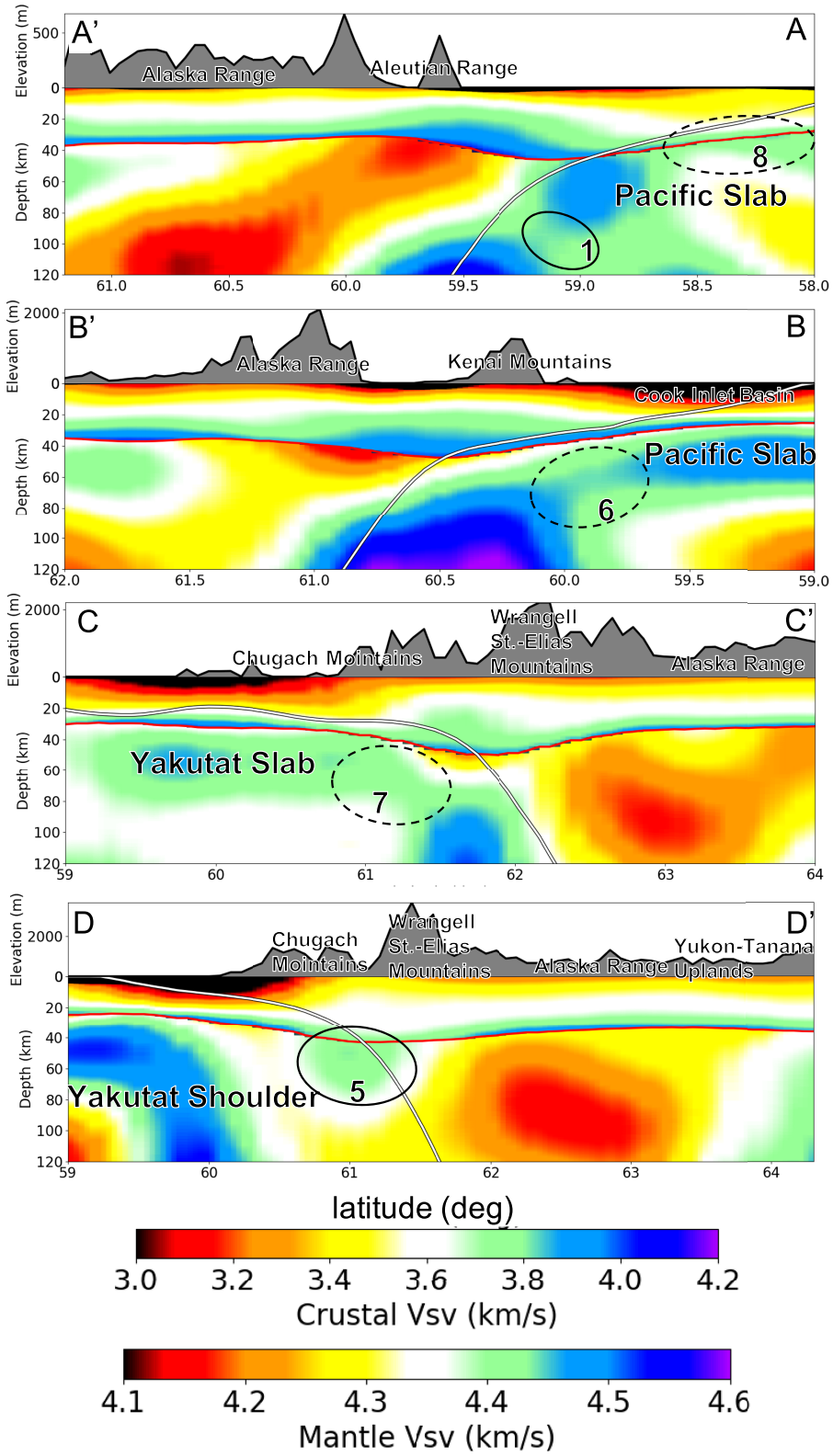

Figure 19. Vertical cross-sections A-A′, B-B′, C-C′, and D-D′ identified in Figure 18. The white lines in the cross-sections identify the upper edge of the subducting lithosphere in the model of Jadamec and Billen (2010). The black oval numbered 1 in profile A-A′ is the Barren Islands slab anomaly, and other ovals are defined in the text. Dashed oval identify features we do not interpret, and the solid ovals are features we do interpret. The red curves indicate the location of Moho.

Similar to Moschetti et al. (2010), we find that there is a trade-off between the values of radial anisotropy in the crust and mantle. As Figure 10 illustrates, mantle radial anisotropy changes appreciably with changes in crustal radial anisotropy. At some locations, mantle radial anisotropy may not be required to fit the data, as illustrated by the points for the Brooks Range and the Cook Inlet in the marginal distributions of Figure 8, but at most locations, crustal or sedimentary anisotropy is needed. We discuss this further in section 6.

5. Results

As described above, the mean model at each grid point ($\overline{m}$) as a function of depth and for the depth to each interface is mean of the posterior distribution, which defines the 3-D *V*sv model as well as the amplitude of radial anisotropy in the crust (γ_c) or sediments (γ_s) and the mantle (γ_m). The standard deviation of the posterior distribution (σ_m) provides a conservative estimate of uncertainty (e.g., Shen & Ritzwoller, 2016). Here, we discuss the characteristics of the 3-D model for isotropic structure and radial anisotropy.

5.1. 3-D Isotropic Model: *V*sv

Figure 11a shows the sedimentary thickness estimates of the mean model. Clearly, the Colville Basin in the Alaskan North Slope region is the most significant basin, but other basins are also resolved in the model and are labeled with numbers in Figure 11a and identified in Table 4. Sedimentary thickness is quite uncertain due to the trade-off with upper crustal shear wave speeds. Shear wave speed at the top of the crystalline crust is also affected by this trade-off, as the uncertainties in Figure 9 illustrate.

The shear wave speed distribution (*V*sv) averaged from the surface of the Earth to a depth of 6 km is presented in Figure 11b. This depth range also displays the imprint of the basins where they exist, but where basins do not exist, it provides an estimate of crustal wave speed in the upper crystalline crust. This figure and those at other depths present slices over a similar depth range ($\pm$3 km).

In the middle crust, near 20-km depth (Figure 11c), the model is better resolved than nearer to the surface, due to fewer trade-offs away from interfaces. However, uncertainty increases dramatically when Moho depth approaches 20 km, which it does near the southern edge of the study region. There is a prominent low velocity lineation running near the major faults bounding the Brooks Range. A low velocity anomaly at this depth also appears near the Chugach-Prince William terrane, in the middle of the Yakutat microplate which is identified by the white polygon in the figure, and near the Wrangell volcanic field. High-velocity anomalies are observed in the crust above the subducting Alaska-Aleutian slab and beneath the North American craton.

Near the bottom of the crust (Figure 11d), the lateral variability of *V*sv is weaker, except for small regions offshore where the crust is thinner than on the continent. The lowest onshore velocities (3.70–3.75 km/s) appear near the major faults bounding the Brooks Range, as they do at 20-km depth, and in the Wrangell volcanic field. The highest velocities (above 3.95 km/s) are found in the interior of the state and in Arctic-Alaska and the North American craton in northern Canada. Uncertainty increases in the lowermost crust because of trade-offs with Moho depth, as Figure 9 shows.

Crustal thickness estimates are presented in Figure 12a and one standard deviation of the posterior distribution in Figure 12b. Crustal thickness is typically poorly constrained by surface wave dispersion data alone, and uncertainties are fairly uniform geographically, averaging about 4–5 km. Nevertheless, our crustal thickness estimates differ substantially from the reference model (Figure 12c) but are similar to those of Miller and Moresi (2018) based on receiver functions (Figure 12d). Details differ, but the large-scale features are similar. Notably, and unsurprisingly, the crust is thicker beneath the Brooks Range and the Alaska Range while it is thinner in the interior of Alaska, for example, the Yukon Composite Terrane. Figure 13 shows a histogram of differences between our model and that of Miller and Moresi (2018), where the mean difference is about 1.5 km (Moho in our model is on average a bit shallower), and the standard deviation of differences is about 3.4 km. Thus, the mean difference between the models is within one standard deviation of the posterior distribution, presented in Figure 12b.

Two horizontal *V*sv slices of the mean model are shown in Figure 14 at depths of 60 km and at 100 km in the mantle. The most prominent positive anomalies are the cratonic roots beneath Artic-Alaska and the North American craton. The edge of the velocity anomaly in Canada forms the so-called Cordillera-Craton boundary. In the interior of Alaska, the mantle is mostly a broad relative low velocity zone. High topography of the

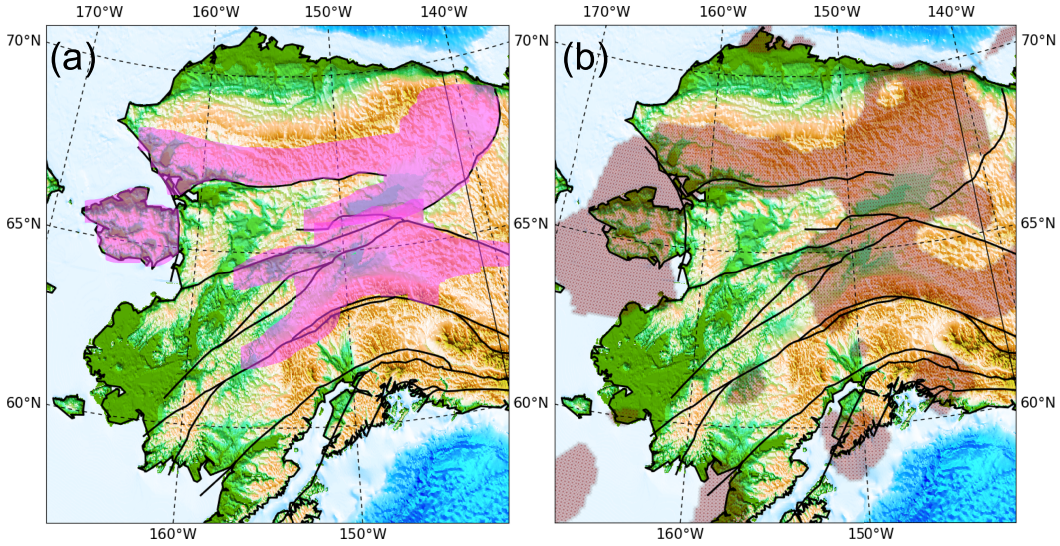

Figure 20. (a) Regions (colored in pink) identified by Miller and Hudson (1991) that have been subjected to significant mid-Cretaceous extension. (b) Regions (colored in brown) where we have confidence that the crustal anisotropy in the final model is considered to be stronger than average ($\gamma_c > 2.6\%$).

Brooks Range, the Alaska Range, and other ranges is not underlain uniformly by low velocity uppermost mantle, which has implications for the nature and depth extent of isostasy (e.g., Levandowski et al., 2014). The Wrangell volcanic field at 60 km is underlain by low velocities in the mantle, particularly offset north of the volcanoes. The back-arc area northwest of the Alaska-Aleutian subduction zone displays low velocity features in the supra-slab wedge that encompass the volcanoes at 60-km depth but which is offset further to the northwest at greater depths. Subducting lithosphere is imaged clearly at 100 km, but at 60 km, it is mainly offshore along the Alaska-Aleutian subduction zone and not as well resolved. The nature of subducting lithosphere in the 3-D model is discussed in greater detail in section 6.

5.2. 3-D Model of Radial Anisotropy: γ_c,γ_m

5.2.1. Data Fit as a Function of Model Parameterization

Data misfit, defined by equation (3), for various models is shown in Figure 15. For the data to be considered fit well, a value of misfit below about 2.0 should be achieved. Figure 15a shows the misfit for the isotropic model, in which Vsh = Vsv so that $\gamma_s = \gamma_c = \gamma_m = 0$. This map reveals the Rayleigh-Love discrepancy. Across most of Alaska the Rayleigh and Love wave dispersion data cannot be fit simultaneously with an isotropic model, and average misfit (equation (3)) is 2.41.

As discussed in section 4.3, there is a substantial trade-off between crustal and mantle anisotropy that broadens the posterior distribution for both γ_c and γ_m, but reliable simultaneous estimates of these variables are possible in most places. However, due to the exceptionally large anisotropy, γ_s, in the Colville Basin, we cannot estimate γ_c reliably. In this basin, we allow anisotropy in the sediments and mantle but not in the crystalline crust (i.e., $\gamma_c = 0, \gamma_s \neq 0 \neq \gamma_m$), but outside the basin, the model includes anisotropy in the crystalline crust and mantle but not the sediments (i.e., $\gamma_s = 0, \gamma_c \neq 0 \neq \gamma_m$). The resulting data misfit is shown in Figure 15b. With the model including mantle and crustal (or sedimentary) radial anisotropy, the data can be fit across the entire region of study with an average misfit of 0.78.

Without sedimentary or crystalline crustal anisotropy but including mantle anisotropy ($\gamma_s = \gamma_c = 0, \gamma_m \neq 0$), the misfit is shown in Figure 15c. The average misfit is 1.40, and across much of Alaska, there is a large residual misfit, particularly in the parts of the state north of the Denali fault. This includes the Colville basin, as well as the area along the Brooks Range and the region between the Denali and Tintina faults focused broadly on the Yukon Composite Terrane. Thus, to achieve acceptable data fit, crustal anisotropy must be introduced in the crystalline crust or the sediments of the Colville Basin. Figure 15d presents the misfit from the inversion that includes sedimentary or crustal anisotropy but not mantle anisotropy (i.e., $\gamma_m = 0, \gamma_s \neq 0$ or $\gamma_c \neq 0$). The misfit value drops dramatically when introducing crustal anisotropy (from 1.40 to 0.78) and increases only moderately when turning off mantle anisotropy (from 0.78 to 0.95). Thus, the primary

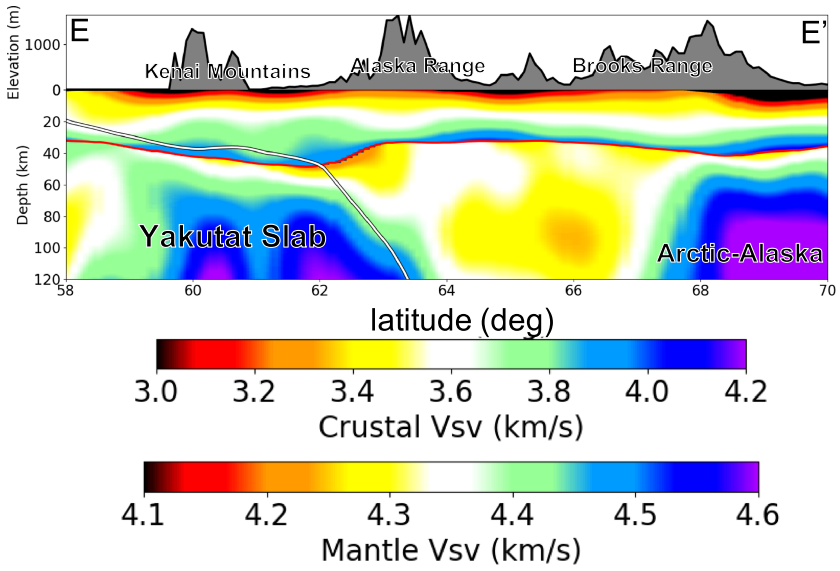

Figure 21. Vertical cross-section E-E′ identified in Figure 14b. The white lines in the cross-sections identify the upper edge of the subducting lithosphere in the model of Jadamec and Billen (2010). The red curve indicates the location of Moho.

factor that determines data fit is actually crustal anisotropy (and in Colville Basin sedimentary anisotropy). Mantle anisotropy can be determined reliably even though its effect on the Rayleigh-Love discrepancy is weaker.

Figure 16 illustrates in greater detail the improvement in fitting the Rayleigh-Love discrepancy. The error bars in this figure are for differences in observed Love wave phase speed and Rayleigh wave phase speed at four locations for our final model ($\gamma_m \neq 0, \gamma_c \neq 0$ or $\gamma_s \neq 0$). The dashed line indicates the fit to this difference based on the isotropic model at each location, where $V\text{sv} = V\text{sh}$ ($\gamma_s = \gamma_c = \gamma_m = 0$). There are large period-dependent discrepancies between the line predicted by the isotropic model and the observations. Beneath the Brooks Range and Cook Inlet, the discrepancy is approximately constant across period, implying that radial anisotropy is probably about the same in both the crust and mantle. In contrast, in the Aleutian Back-Arc region, the discrepancy is larger at longer periods so that mantle anisotropy is probably stronger than crustal anisotropy, and in the Yukon Composite Terrane, the discrepancy is greater at shorter periods indicating that crustal anisotropy is probably larger than mantle anisotropy there. In each of these cases, introducing radial anisotropy that is constant with depth separately in the crust and mantle allows the data to be fit well.

5.2.2. The Model of Apparent Radial Anisotropy

The resulting estimates of crustal and mantle anisotropy are shown in Figure 17. We consider estimates of γ_c to be indeterminate if the standard deviation of the posterior distribution for γ_c is greater than 1.0% or in the Colville Basin where we estimate γ_s rather than γ_c. Estimates of γ_m are considered indeterminate if the standard deviation of the posterior distribution is greater than 1.5%. γ_m has a weaker impact on the Rayleigh-Love discrepancy than γ_c, so we make the tolerance broader for mantle anisotropy than for crustal anisotropy.

Crustal anisotropy is on average stronger than mantle anisotropy and more geographically variable. Mantle anisotropy is somewhat more homogeneous than crustal anisotropy, and the patterns of crustal and mantle anisotropy are generally complementary. In this latter respect, crustal and mantle anisotropy may have formed in response to different episodes of tectonic strain. In particular, the geographical distribution of crustal anisotropy corresponds in part to areas of significant crustal extension, as discussed further in section 6.3.

6. Discussion

6.1. Radial Anisotropy of the Colville Basin

The North Slope foreland basin, or the Colville Basin or trough, is a late Mesozoic and Cenozoic basin that runs from the Brooks Range in the south to the edge of the Beaufort Sea in the north (e.g., Bird & Molenaar,

1992). The basin is about 1,000 km long and 50 to 350 km wide and is by far the largest basin in the region of study. We approximate its extent with the 2.5 km/s contour on the 10-s Rayleigh wave group speed map (Figure 3d).

As indicated by the *V*sv and *V*sh profiles shown for a point in the Colville Basin in Figure 7b, the radial anisotropy in the sediments of the basin is much stronger than across the crystalline crust. Values of sedimentary apparent radial anisotropy average in excess of 20% throughout the basin, similar to the large values reported by Xie et al. (2013) for the Sichuan Basin. The stratification and layering found in sedimentary basins probably generate this strong radial anisotropy. Our model cannot provide information about the layering of structures in basins, but we are confident that the anisotropy (γ_s) in the Colville Basin is exceptionally strong, much stronger than either crustal or mantle radial anisotropy (γ_c,γ_m). Additional data, such as receiver functions or Rayleigh wave H/V ratio, which are more sensitive to the shallowest parts of the Earth and also provide better constraints on sediment thickness, may help to improve sedimentary structures, helping to provide better information about sedimentary anisotropy.

6.2. Resolved Subducted Lithosphere

Resolving subducted lithosphere including accurately capturing the geometry of the subducting slab, its thickness, and the amplitude of velocities in the slab is very challenging for inversions based on surface wave data alone for the following reasons. (1) Surface waves in general have better depth resolution than horizontal resolution. Consequently, the ability to determine lithospheric thickness varies with the dip angle of the slab. Slab thickness is better constrained when the lithosphere is horizontal, but as the dip angle increases, the ability to determine slab thickness degrades appreciably. (2) A particular complication for our study is that a significant part of the Alaskan subduction zone is located at the southern edge of our model, which is offshore with poor path coverage for ambient noise data and no data coverage for earthquakes. Therefore, at least offshore, we lack dispersion measurements at the longer periods (indicated in Figure 3), which reduces confidence in structures deeper than about 100 km. Shorter period dispersion measurements are also affected by reduced data coverage, which makes it harder to recover the amplitude of velocity anomalies correctly. Despite these issues, aspects of the subducting lithosphere at depths above about 100 km can be resolved reliably. In particular, we are able to resolve the top of the subducting slab above 100-km depth and its areal extent, especially in onshore regions.

Figure 18 indicates some of the features associated with subduction zone at 100-km depth with corresponding uncertainties. The uncertainty map presents one standard deviation of the posterior distribution. As Shen and Ritzwoller (2016) pointed out, one standard deviation of the posterior distribution is probably be an overly conservative estimate of uncertainty but does capture an estimate of the relative reliability of the resulting model. The average one standard deviation of the posterior distribution at 100-km depth, as indicated in Figure 9, is ~70 m/s. The uncertainty map (Figure 18b) indicates larger values (>70 m/s) in the southern periphery region of the subduction zone, while the uncertainties for the back-arc areas are appreciably smaller than average (~70 m/s). This is caused by the fact that path coverage is sparser offshore.

To illuminate the well-resolved features, we begin by comparing the 3-D *V*sv model (mean of the posterior distribution) with two prominent slab models that delineate Alaskan subduction zones: Slab1.0 by Hayes et al. (2012) and the Alaska_3D 1.0 model by Jadamec and Billen (2010). These two models are generally consistent in depicting the Alaska-Aleutian subduction zone comprising dashed boxes A and B in Figure 18a, which we call Blocks A and B. Slab edges from these models at 100-km depth are presented in this figure with the dashed red and solid cyan curves. However, unlike Slab1.0, the Alaska_3D 1.0 model also includes a slab kink near the Denali fault and the northern-most edge of the Denali volcanic gap, and the slab extends into what we refer to as the Yakutat subduction zone in Block C and beyond. Because our 3-D model also includes the slab kink (Figure 18a) near the Denali fault (Block B) and the subducting Yakutat slab (Block C), we will concentrate comparison of our model with Alaska_3D 1.0.

Following the cyan slab edge curve at 100-km depth from the west to the east in Figure 18a, we divide the Alaskan subduction zone into four structurally distinct blocks: Blocks A–D. They are identified with letters in Figure 18a as (A) the Aleutian subduction zone, (B) the Alaskan subduction zone and slab edge or kink, which includes the Denali volcanic gap, (C) the Yakutat subduction zone, and (D) the Yakutat slab shoulder.

In the Aleutian subduction zone (Block A), the edge of the high-velocity Pacific slab is consistent with the slab edge curves of both the Slab 1.0 and Alaska_3D 1.0 models. The location of the slab in our model also generally matches the locations of the Aleutian volcanic arc (white triangles) and earthquakes in the depth range near 100 km (yellow dots). We also note that there is an anomaly in slab structure (identified as Oval 1 in Figure 18a) located near the Barren Islands in the strait between the Kenai Peninsula and Kodiak Island. This is what we call the "Barren Islands slab anomaly," which is a notable reduction in shear wave speed at 100-km depth and occurs in a region of heightened seismicity at this depth. Profile A-A′ in Figure 19 extends across the Barren Islands anomaly and shows the anomaly in cross-section (black oval labeled with the number 1 in the A-A′ cross-section) as a reduction in shear wave speed in a confined depth range that occurs adjacent to very slow velocity supra-slab wedge in the back-arc. In contrast, profile B-B′ in Figure 19 extends through a more normal section of the subducting lithosphere, in which no low velocity anomaly appears and the back-arc is not as slow. Yang and Gao (2018) also report a low velocity region in the uppermost mantle near the Barren Islands and refer to it as a "slab gap" characteristic of horizontal slab segmentation and perhaps a slab tear. In contrast, we image this as a vertically confined anomaly, so we do not refer to it as a gap and do not image a structure that is consistent with slab segmentation or a tear that extends across a significant depth range. Consequently, we hypothesize that the Barren Islands slab anomaly reflects slab heating caused by higher temperatures and perhaps fluid or melt in the back-arc region localized near 100-km depth. However, the Barren Islands slab anomaly may result from failing to recover the full amplitude of the positive anomaly within the slab. Indeed, as the uncertainty map (Figure 18b) indicates, the one standard deviation of the posterior distribution for this location is relatively large (~80 m/s). Further efforts are warranted to improve the vertical and horizontal resolution of this intriguing lithospheric feature in order to clarify its physical cause.

The Alaskan subduction zone ends northward to a slab edge or kink, which is identified as the edge of Block B in Figure 18a. Rondenay et al. (2010) propose that the Denali Volcanic Gap is caused by the cooling effect of the Yakutat slab, which essentially reduces melt production and hinders magma ascent to the surface. However, we observe a low velocity zone in the mantle wedge beneath the Denali Volcanic Gap that is similar to cross-sections A′-A and B′-B that show the mantle wedge structures beneath volcanogenic regions. The low velocity anomaly supports the existence of serpentinization in the mantle wedge beneath both volcanic and nonvolcanic zones, which is suggested by Ward and Lin (2018) and Martin-Short et al. (2018). Others have argued that the kink structure may result in toroidal mantle flow around it, and the flow pattern predicted by the geodynamical model of Jadamec and Billen (2010) is consistent with SKS splitting studies (e.g., Christensen & Abers, 2010; Hanna & Long, 2012; Perttu et al., 2014).

Oval 2 located northeast of Block B in Figure 18a is a high-velocity extension to the slab edge, which was suggested to be an aseismic slab edge by Gou et al. (2019). This aseismic slab edge has slightly larger uncertainties than in surrounding areas, as illustrated in Figure 18b. However, it has also been imaged by Wang and Tape (2014), Jiang et al. (2018), and Martin-Short et al. (2018).

Moving eastward along the slab edge from the slab kink to the Yakutat subduction zone, Block C in Figure 18a, there is another relative low velocity anomaly (Oval 3) located northwest of the Wrangell Volcanic Field (Oval 4). This "Wrangellia slab anomaly," as we call it, has larger uncertainties than adjacent back-arc areas, as indicated by Figure 18b. However, this feature is also captured by the *V*p model of Gou et al. (2019) at a similar depth. Observations of tectonic tremors (Wech, 2016) reported that interevent times increase from ~10 days in the west to ~3 hr in the east of this location. Because we see no evidence of subduction continuing to the east of the slab edge in the Yakutat subduction zone (Block C), similar to Martin-Short et al. (2018), we suggest that the increase in tremor frequency could be explained by the heating of the slab edge by the adjacent hot back-arc materials. The vertical cross-section C-C′ in Figure 19 shows that the high-speed anomaly in Block C appears to be part of the subducting Yakutat slab and occurs at the location of the slab in model Alaska_3D 1.0. Previous studies based on earthquake locations (Page et al., 1989) indicate a transition from shallow to steep dip angle for this part of slab at ~70-km depth. We observe a similar transition in dip angle of the slab in the cross-section C-C′. Therefore, similar to Jiang et al. (2018), we suggest that this part of the slab is sinking vertically because the subduction is slowed down by the Yakutat collision. Martin-Short et al. (2018) observed a horizontal Yakutat LAB below the Wrangell volcanic field at a depth around 100 km, which is different from the vertical sinking feature imaged by our model and Jiang et al. (2018).

The Yakutat slab is older than the Pacific slab (e.g., Eberhart-Phillips et al., 2006) and thus physically should be thicker. This, however, is hard to test with our model. By comparing cross-section C-C′ with cross-sections B′-B and A′-A, we note that the thickness of the shallowly dipping part of the Pacific slab is less than ~80 km while it is hard to tell the exact thickness of the Yakutat slab. At ~100-km depth for the Yakutat Slab in cross-section C-C′, the values of Vsv are ~4.35 km/s, with corresponding values of uncertainties that may be as large as ~80 m/s (Figure 18b). This confounds the determination of the thickness of the Yakutat slab and the determination if Yakutat slab is thicker than the Pacific slab.

As illustrated in Figure 18a, there is an increasing mismatch in slab geometry between our model and Alaska_3D 1.0 as the edge of Yakutat slab extends southeastward into what we refer to as the "Yakutat slab shoulder" region (Block D). The corresponding vertical cross-section D-D′ in Figure 19 shows a high-speed anomaly seaward of the Chugach Mountains rather than near the slab edge predicted by the model Alaska_3D 1.0. This anomaly is separated from another high-speed anomaly identified by Oval 5 in D-D′, which is in the slab shoulder region of the Yakutat slab. The uncertainty map in Figure 18b indicates that the Yakutat slab shoulder may not be constrained as well as other features that we image in the subduction zone. There is, however, evidence that this region may be an isolated block that experienced rotational transport. Based on evidence provided by surface geology and Global Positioning System data, Pavlis et al. (2019) suggested that the Yakutat slab shoulder may have experienced block rotation over the past 6 Ma. By projecting this block back 6 Ma, they found that the southern coastline for Alaska would be consistent with the edge of slab imaged by Kim et al. (2014). In this interpretation, the Yakutat slab shoulder would be an isolated block that is distinct from surrounding areas. However, the larger uncertainties for the region mean that the spatial extent of the feature is uncertain. This high-speed Yakutat slab shoulder has not been imaged in previous seismic tomography studies.

In closing, we note several features that appear in the vertical cross-sections that we do not feel justified interpreting. These features are either located in the periphery of the region of study or deeper than 100-km depth, where uncertainty is relatively large. (1) The amplitudes of the high-speed anomalies weaken where the slab begins to subduct in cross-sections B-B′ and C-C′, marked with Ovals 6 and 7. This may be due to the difficulty in recovering amplitudes correctly due to poor data coverage at those locations, which reduces our confidence in these features. (2) The slab thickens and the slab edge increasingly mismatches the Alaska_3D 1.0 model below 100-km depth on vertical cross-sections A-A′ and particularly B-B′, which we believe are artifacts caused by degradation in resolution with depth. Introducing body wave data sets may potentially help in better resolving the deeper part (>100 km) of the subduction zone, which is beyond the scope of this study. (3) Oval 8 in profile A-A′ is an offshore region where we are unable to resolve uppermost mantle structure reliably.

6.3. Extensional Provinces and Radial Anisotropy

Crustal radial anisotropy (γ_c) averages about 2.6% in our 3-D model (Figure 17a). It is strongest (>2.6%) across a broad swath of central and northern Alaska, including the Seward Peninsula, the southern parts of Brooks Range, the Ruby Terrane, and the Yukon Composite Terrane, as shown in Figure 20b. Miller and Hudson (1991) identified regions in Alaska that were subjected to significant Cretaceous ductile extension, which they refer to as the "hinterland" of the Brooks Range fold and thrust belt. The regions that they believe constitute the basement during the extensional episodes are shown schematically in Figure 20a. These extensional regimes are nearly coincident with the areas of strong crustal radial anisotropy that we image.

Crustal radial anisotropy also has been observed in other regions that have or are undergoing extensional deformation, including in Tibet (Shapiro et al., 9 July 2004; Xie et al., 2013) and the Basin and Range province of the western United States (Moschetti et al., 2010). The results we present here support the hypothesis developed in these earlier studies that deformation in the crystalline crust dominantly controls the formation of apparent radial anisotropy and conversely that apparent radial anisotropy is a marker for crustal extension. Such anisotropy may result from the formation of middle to lower crustal sheet silicates (micas) with shallowly dipping foliation planes beneath extensional domains (e.g., Hacker et al., 2014). Xie et al. (2017) propose that the depth range of the deformation that is causing apparent radial anisotropy lies in the middle to lower crust, but we do not have the depth resolution to test this hypothesis.

6.4. Cratons and Thickened Lithosphere

The horizontal profiles of Figure 14 illustrate similarity between the uppermost mantle beneath Arctic-Alaska and the North American (or Laurentian) craton to the east. Both appear as very high velocity features that extend at least to 120-km depth (e.g., Figure 21, profile E-E′) and presumably deeper, although we are unable to resolve features reliably below 120 km. Thus, the seismic evidence is quite clear that Arctic-Alaska appears to be underlain by very thick lithosphere that is possibly cratonic in nature.

Moore and Box (2016) describe several prominent models for the tectonic origin of Arctic-Alaska and the arrangement of terranes. These models include those in which Arctic-Alaska has maintained a fixed position relative to North America throughout Phanerozoic time and those they describe as more popular models that involve a large-scale counter-clockwise rotation and transport of Arctic-Alaska as part of the rotational opening of the Canada Basin in the Early Cretaceous. Kinematic models of the tectonic formation of Arctic-Alaska should consider that this region is underlain by very thick lithosphere that could inhibit large-scale transport or rotation. Other regions with fast and thick lithosphere situated in the presence of significant continental deformation, such as the Tarim Basin (e.g., Molnar & Tapponnier, 1981), the Sichuan Basin (e.g., Klemperer 2006), and the Ordos Block in Asia, appear to impede crustal flow and not participate in the surrounding deformational processes except near their margins. Thus, the thick lithosphere of Arctic-Alaska challenges rotational transport models and may be more consistent with fixist models of the evolution of the region. Alternately, the high-mantle velocities could result from lithosphere that subducted during the formation of the Brooks Range and foundered afterwards. Attempting to resolve this dichotomy is beyond the scope of this paper.

Close inspection of Figures 14a and 14b reveals that the high-velocity anomalies beneath Arctic-Alaska extend under the Brooks Range and move southward with increasing depth. This can be seen more clearly in vertical profile E-E′ shown in Figure 21, where it appears that the upper mantle underlying the region underthrusts the Brooks Range. The geometry of the thick lithosphere relative to the location of the Brooks Range provides additional information for tectonic reconstructions of the region. Jiang et al. (2018) also image high velocities in the mantle beneath Arctic-Alaska, which appear to extend further southward at greater depths.

7. Conclusions

We present a radially anisotropic 3-D model of *V*sv and *V*sh for the crust and uppermost mantle to a depth of 120 km beneath Alaska and its surroundings using Rayleigh wave group and phase speed and Love wave phase speed measurements. We acquire waveforms from all broadband seismic stations across the study region openly available from January 2001 to February 2019, totaling more than 500 stations taken from 22 networks (Transportable Array, Alaska Networks, etc.), to perform both ambient noise and earthquake tomography. Rayleigh wave phase speed maps extend from 8- to 85-s period whereas the group speed maps and the Love wave phase speed maps range from 8 to 50 s. These data and corresponding uncertainties are the basis for the inversion for the 3-D model across the study region.

The 3-D model derives from a Bayesian Monte Carlo procedure applied on a grid spacing of approximately 50 km. The prior distribution spans broad bounds around the reference model, in which the sedimentary characteristics and Moho depth come from CRUST-1.0 and crustal and mantle wave speeds come from 1-D model ak135. Constraints limit the accepted models to be vertically smooth between interfaces and relatively simple, which is a hypothesis that is tested in the inversion. The inversion results in a posterior distribution of models beneath each grid point, which we summarize at each point and depth with the mean ($\overline{m}$), which we refer to as the "mean model," and standard deviation (σ_m), which we refer to as "uncertainty." Shen and Ritzwoller (2016) argue that σ_m is not an ideal estimate of absolute model uncertainty, as it overestimates nonsystematic error and does not explicitly quantify systematic error, but it does provide information about relative uncertainty. We find that we can constrain the shear wave structures relatively well in the middle of the crust and mantle, but internal interfaces are not determined as accurately.

For the vast majority of the region of study, the average model fits the dispersion data well with misfit χ (equation (3)) smaller than 2.0 for our final mean model. The data cannot be fit without introducing apparent radial anisotropy, but a very simple parameterization in which mantle and crustal radial anisotropy are

spatially variable but respectively constant with depth at each point suffices to fit the data. Crustal anisotropy is represented either with a depth-constant value in the crystalline crust (γ_c) or sediments (γ_s) depending on sedimentary thickness. Typically, $\gamma_s \gg \gamma_c > \gamma_m$, with values of γ_s (determined only in the Colville Basin) being greater than 20%, and values of γ_c and γ_m running up to 8% depending on location. With the current data set we are not justified in inferring a model that possesses more vertical variability of apparent radial anisotropy.

Many structural features are determined reliably in the final 3-D model, and we mention a few in this paper. (1) Apparent crustal radial anisotropy is strongest across a broad swath of central and northern Alaska, coincident with areas identified by Miller and Hudson (1991) that were subjected to significant Cretaceous extensional deformation. (2) Apparent radial anisotropy in the sediments of the Colville basin is very strong, presumably caused by sedimentary stratification and layering. (3) Crustal thickness estimates are similar to those based on receiver functions by Miller and Moresi (2018). (4) The uppermost mantle beneath Arctic-Alaska is a high-velocity feature that extends at least to 120-km depth, which may be more consistent with fixist models for the evolution of the region than more popular rotational transport models. (5) The slab geometry of the Alaskan subduction zone that we image is largely consistent with the Alaska_3D 1.0 model of Jadamec and Billen (2010), with the principal exception being what we call the "Yakutat slab shoulder region." Our model also confirms the existence of structural features that have been reported by recent studies, including what we call the "Barren Islands slab anomaly" which is a relative low velocity anomaly in the upper mantle that was also observed by Yang and Gao (2018), the "Alaskan aseismic slab edge" that was also observed by Jiang et al. (2018) and Gou et al. (2019), the "Wrangellia slab anomaly" that was also imaged by Gou et al. (2019), and subducting Yakutat lithosphere seaward of the Wrangell volcanic field (Gou et al., 2019; Jiang et al., 2018; Martin-Short et al., 2018). The "Yakutat slab shoulder region" is a high-speed anomaly in our model in the upper mantle, which has not been reported in previous tomography studies. Pavlis et al. (2019) suggested that Yakutat slab shoulder experienced a block rotation over the past 6 Ma.

The 3-D model presented here should be a useful reference for a variety of purposes, including for earthquake location and predicting other types of geophysical data. However, future work is needed to continue to improve both the *V*sv and *V*sh parts of the model. For example, observations of the Rayleigh wave *H*/*V* ratio would help to improve the shallowest parts of the model, and receiver functions may be added to help refine internal interfaces. However, receiver functions in Alaska are often complicated and strongly spatially variable, similar in many respects to those in Tibet even though the Tibetan crust is much thicker. The multistation common Moho conversion point stacking method (e.g., Deng et al., 2015) may yield better information than single-station based stacking or harmonic stripping methods such as those applied across the lower 48 states by Shen and Ritzwoller (2016), for example. There are many other fertile directions to pursue in order to improve and extend the model, but we mention only one more. Once Rayleigh wave azimuthal anisotropy is estimated, those measurements can be added to the data presented here to invert for an integrated model of inherent anisotropy represented by the depth-dependent tilted elastic tensor, as described by Xie et al. (2015, 2017).

Acknowledgments
The authors thank two anonymous reviewers and the Associate Editor, Sébastien Chevrot, for constructive comments that helped improve the quality of this paper. They are also grateful to Craig Jones, Anne Sheehan, and Shijie Zhong for helpful comments. This research was supported by National Science Foundation Grant EAR-1928395 at the University of Colorado at Boulder. The facilities of IRIS Data Services (https://www.iris.edu/), and specifically the IRIS Data Management Center, were used for access to waveforms, related metadata, and/or derived products used in this study. IRIS Data Services are funded through the Seismological Facilities for the Advancement of Geoscience and EarthScope (SAGE) Proposal of the National Science Foundation under Cooperative Agreement EAR-1261681. The network codes for data that are used include 5C, 7C, AK, AT, AV, CN, II, IU, PN, PO, PP, TA, US, XE, XN, XR, XY, XZ, YE, YM, YV, and ZE. A description of the seismic networks is found in Table 2. This work utilized the RMACC Summit supercomputer, which is supported by the National Science Foundation (Awards ACI-1532235 and ACI-1532236), the University of Colorado Boulder, and Colorado State University. The Summit supercomputer is a joint effort of the University of Colorado Boulder and Colorado State University. The anisotropic model presented in this paper can be accessed online (https://github.com/NoisyLeon/ALASKA_radial_mod).

References

Allam, A. A., Schulte-Pelkum, V., Ben-Zion, Y., Tape, C., Ruppert, N., & Ross, Z. E. (2017). Ten kilometer vertical Moho offset and shallow velocity contrast along the Denali fault zone from double-difference tomography, receiver functions, and fault zone head waves. *Tectonophysics*, *721*, 56–69. https://doi.org/10.1016/j.tecto.2017.09.003

Amante, C. and Eakins, B.W. (2009). ETOPO1 arc-minute global relief model: Procedures, data sources and analysis.

Babuska, V., & Cara, M. (1991). *Seismic anisotropy in the Earth* (Vol. 10). *Springer Science & Business Media*.

Barmin, M. P., Ritzwoller, M. H., & Levshin, A. L. (2001). A fast and reliable method for surface wave tomography. *Pure and Applied Geophysics*, *158*(8), 1351–1375. https://doi.org/10.1007/PL00001225

Bensen, G. D., Ritzwoller, M. H., Barmin, M. P., Levshin, A. L., Lin, F., Moschetti, M. P., et al. (2007). Processing seismic ambient noise data to obtain reliable broad-band surface wave dispersion measurements. *Geophysical Journal International*, *169*, 1239–1260. https://doi.org/10.1111/j.1365-246X.2007.03374.x

Bird, K. J., & Molenaar, C. M. (1992). In R. W. Macqueen & D. A. Leckie (Eds.), Ch. 13*The North Slope foreland basin, Alaska, in foreland basins and fold belts* (pp. 363–393). American Association of Petroleum Geologists. https://doi.org/10.1306/M55563

Brennan, P. R., Gilbert, H., & Ridgway, K. D. (2011 Apr). Crustal structure across the central Alaska Range: Anatomy of a Mesozoic collisional zone. *Geochemistry, Geophysics, Geosystems*, *12*, Q04010. https://doi.org/10.1029/2011GC003519

Brocher, T. M. (2005). Empirical relations between elastic wave speeds and density in the Earth's crust. *Bulletin of the Seismological Society of America*, *95*, 2081–2092. https://doi.org/10.1785/0120050077

Christensen, D. H., & Abers, G. A. (2010). Seismic anisotropy under central Alaska from SKS splitting observations. *Journal of Geophysical Research*, *115*, B04315. https://doi.org/10.1029/2009JB006712

Coney, P. J., & Jones, D. L. (1985). Accretion tectonics and crustal structure of Alaska. *Tectonophysics*, *119*(1-4), 265–283. https://doi.org/10.1016/0040-1951(85)90042-3

Deng, Y., Shen, W., Xu, T., & Ritzwoller, M. H. (2015). Crustal layering in northeastern Tibet: A case study based on joint inversion of receiver functions and surface wave dispersion. *Geophysical Journal International*, *203*(1), 692–706. https://doi.org/10.1093/gji/ggv321

Eberhart-Phillips, D., Christensen, D. H., Brocher, T. M., Hansen, R., Ruppert, N. A., Haeussler, P. J., & Abers, G. A. (2006). Imaging the transition from Aleutian subduction to Yakutat collision in central Alaska, with local earthquakes and active source data. *Journal of Geophysical Research*, *111*, B11303. https://doi.org/10.1029/2005JB004240

Ekstrom, G., & Dziewonski, A. M. (1998). The unique anisotropy of the Pacific upper mantle. *Nature*, *394*(6689), 168–172. https://doi.org/10.1038/28148

Erdman, M. E., Hacker, B. R., Zandt, G., & Seward, G. (2013). Seismic anisotropy of the crust: Electron-backscatter diffraction measurements from the basin and range. *Geophysical Journal International*, *195*(2), 1211–1229. https://doi.org/10.1093/gji/ggt287

Feng, L., & Ritzwoller, M. H. (2017). The effect of sedimentary basins on surface waves that pass through them. *Geophysical Journal International*, *211*(1), 572–592. https://doi.org/10.1093/gji/ggx313

Ferris, A., Abers, G. A., Christensen, D. H., & Veenstra, E. (2003). High resolution image of the subducted Pacific (?) plate beneath central Alaska, 50-150 km depth. *Earth and Planetary Science Letters*, *214*(3-4), 575–588. https://doi.org/10.1016/S0012-821X(03)00403-5

Freymueller, J. T., Woodard, H., Cohen, S. C., Cross, R., Elliott, J., Larsen, C. F., et al. (2008). Active deformation processes in Alaska, based on 15 years of GPS measurements. In *Active Tectonics and Seismic Potential of Alaska*, Geophysical Monograph Series (Vol. 179, pp. 1–42). Washington, DC: AGU.

Fuis, G. S., Levander, A. R., Lutter, W. J., Wissinger, E. S., Moore, T. E., & Christensen, N. I. (1995). Seismic images of the Brooks Range, Arctic Alaska, reveal crustal-scale duplexing. *Geology*, *23*(1), 65–68. https://doi.org/10.1130/0091-7613(1995)023<0065:SIOTBR>2.3.CO;2

Fuis, G. S., Moore, T. E., Plafker, G., Brocher, T. M., Fisher, M. A., Mooney, W. D., et al. (2008). Trans-Alaska crustal transect and continental evolution involving subduction underplating and synchronous foreland thrusting. *Geology*, *36*(3), 267–270. https://doi.org/10.1130/G24257A.1

Gou, T., Zhao, D., Huang, Z., & Wang, L. (2019). Aseismic deep slab and mantle flow beneath Alaska: Insight from anisotropic tomography. *Journal of Geophysical Research: Solid Earth*, *124*, 1700–1724. https://doi.org/10.1029/2018JB016639

Hacker, B. R., & Abers, G. A. (2004). Subduction Factory 3: An Excel worksheet and macro for calculating the densities, seismic wave speeds, and H_2O contents of minerals and rocks at pressure and temperature. *Geochemistry, Geophysics, Geosystems*, *5*, Q01005. https://doi.org/10.1029/2003GC000614

Hacker, B. R., Ritzwoller, M. H., & Xie, J. (2014). Central Tibet has a partially melted, mica-bearing crust. *Tectonics*, *33*, 1408–1424. https://doi.org/10.1002/2014TC003534

Hanna, J., & Long, M. D. (2012). SKS splitting beneath Alaska: Regional variability and implications for subduction processes at a slab edge. *Tectonophysics*, *530-531*, 272–285. https://doi.org/10.1016/j.tecto.2012.01.003

Hayes, T., Wald, D., & Johnson, R. L.(2012). Slab1.0: A three-dimensional model of global subduction zone geometries. *Journal of Geophysical Research*, *117*, B01302. https://doi.org/10.1029/2011JB008524

Haynie, K. L., & Jadamec, M. A. (2017). Tectonic drivers of the Wrangell block: Insights on fore-arc sliver processes from 3-D geodynamic models of Alaska. *Tectonics*, *36*, 1180–1206. https://doi.org/10.1002/2016TC004410

Herrmann, R. B. (2013). Computer programs in seismology: An evolving tool for instruction and research. *Seismological Research Letters*, *84*, 1081–1088. https://doi.org/10.1785/0220110096

Jadamec, M. A., & Billen, M. I. (2010). Reconciling surface plate motions with rapid three-dimensional mantle flow around a slab edge. *Nature*, *465*(7296), 338–341. https://doi.org/10.1038/nature09053

Jiang, C., Schmandt, B., Ward, K. M., Lin, F.-C., & Worthington, L. L. (2018). Upper mantle seismic structure of Alaska from Rayleigh and S wave tomography. *Geophysical Research Letters*, *45*, 10,350–10,359.

Johnston, S. T. (2001). The Great Alaskan Terrane Wreck: Reconciliation of paleomagnetic and geological data in the northern Cordillera. *Earth and Planetary Science Letters*, *193*(3-4), 259–272. https://doi.org/10.1016/S0012-821X(01)00516-7

Kennett, B. L. N., Engdahl, E. R., & Buland, R. (1995). Constraints on seismic velocities in the Earth from travel times. *Geophysical Journal International*, *122*(1), 108–124. https://doi.org/10.1111/j.1365-246X.1995.tb03540.x

Kim, Y., Abers, G. A., Li, J., Christensen, D., Calkins, J., & Rondenay, S. (2014). Alaska Megathrust 2: Imaging the megathrust zone and Yakutat/Pacific plate interface in the Alaska subduction zone. *Journal of Geophysical Research: Solid Earth*, *119*, 1924–1941. https://doi.org/10.1002/2013JB010581.

Klemperer, S. L. (2006). Crustal flow in Tibet: A review of geophysical evidence for the physical state of Tibetan lithosphere. In M. P. Searle & R. D. Law (Eds.), *Channel flow, ductile extrusion and exhumation of lower mid-crust in continental collision zones*, *Geol. Soc. Spec. Publ* (Vol. 268, pp. 39–70). London: Geological Society of London.

Kustowski, B., Ekström, G., & Dziewoński, A. M. (2008). Anisotropic shear-wave velocity structure of the Earth's mantle: A global model. *Journal of Geophysical Research*, *113*, B06306. https://doi.org/10.1029/2007JB005169

Laske, G., Masters, G., Ma, Z. & Pasyanos, M. (2013). Update on CRUST1.0—A 1-degree global model of Earth's crust, Geophys. Res. Abstracts, 15, Abstract EGU2013-2658.

Levandowski, W., Jones, C., Shen, W., Ritzwoller, M. H., & Schulte-Pelkum, V. (2014). Origins of topography in the Western US: Mapping crustal and upper mantle density variations using a uniform seismic velocity model. *Journal of Geophysical Research: Solid Earth*, *119*, 2375–2396. https://doi.org/10.1002/2013JB010607

Lin, F.-C., Moschetti, M. P., & Ritzwoller, M. H. (2008). Surface wave tomography of the western United States from ambient seismic noise: Rayleigh and Love wave phase velocity maps. *Geophysical Journal International*, *173*(1), 281–298. https://doi.org/10.1111/j1365-246X.2008.03720.x

Lin, F.-C., & Ritzwoller, M. H. (2011). Helmholtz surface wave tomography for isotropic and azimuthally anisotropic structure. *Geophysical Journal International*, *186*(3), 1104–1120. https://doi.org/10.1111/j.1365-246X.2011.05070.x

Lin, F.-C., Ritzwoller, M. H., & Snieder, R. K. (2009). Eikonal tomography: Surface wave tomography by phase-front tracking across a regional broad-band seismic array. *Geophysical Journal International*, *177*(3), 1091–1110. https://doi.org/10.1111/j.1365-246X.2009.04105.x

Marone, F., Gung, Y., & Romanowicz, B. (2007). Three-dimensional radial anisotropic structure of the North American upper mantle from inversion of surface waveform data. *Geophysical Journal International*, *171*(1), 206–222. https://doi.org/10.1111/j.1365-246X.2007.03465.x

Martin-Short, R., Allen, R., Bastow, I. D., Poritt, R. W., & Miller, M. S. (2018). Seismic imaging of the Alaska subduction zone: Implications for slab geometry and volcanism. *Geochemistry, Geophysics, Geosystems*, *19*, 4551–4560. https://doi.org/10.1029/2018GC007962

Martin-Short, R., Allen, R. M., & Bastow, I. D. (2016). Subduction geometry beneath south central Alaska and its relationship to volcanism. *Geophysical Research Letters*, *43*, 9509–9517. https://doi.org/10.1002/2016GL070580

Miller, E. L., & Hudson, T. L. (1991). Mid-Cretaceous extensional fragmentation of the Jurassic-Early Cretaceous compressional orogeny, Alaska. *Tectonics*, *10*(4), 781–796. https://doi.org/10.1029/91TC00044

Miller, M. S., & Moresi, L. (2018). Mapping the Alaskan Moho. *Seismological Research Letters*, *89*(6), 2439–2436. https://doi.org/10.1785/0220180222

Miller, M. S., O'Driscoll, L., Poritt, R. W., & Roeske, S. M. (2018). Multiscale crustal architecture of Alaska inferred from P receiver functions. *Lithosphere*, *10*(2), 267–278. https://doi.org/10.1130/L701.1

Molnar, P., & Tapponnier, P. (1981). A possible dependence of tectonic strength on the age of the crust in Asia. *Earth and Planetary Science Letters*, *52*(1), 107–114. https://doi.org/10.1016/0012-821X(81)90213-2

Montagner, J. P., & Tanimoto, T. (1991). Global upper mantle tomography of seismic velocities and anisotropies. *Journal of Geophysical Research*, *96*(20), 337–20,351. https://doi.org/10.1029/91JB01890

Moore, T. E., & Box, S. E. (2016). Age, distribution, and style of deformation in Alaska north of 60 N: Implications for assembly of Alaska. *Tectonophysics*, *691*, 133–170. https://doi.org/10.1016/j.tecto.2016.06.025

Moschetti, M. P., Ritzwoller, M. H., & Lin, F. C. (2010). Seismic evidence for widespread crustal deformation caused by extension in the western USA. *Nature*, *464*(7290), 885–889. https://doi.org/10.1038/nature08951

Mosegaard, K., & Tarantola, A. (1995). Monte Carlo sampling of solutions to inverse problems. *Journal of Geophysical Research*, *100*(B7), 12,431–12,447. https://doi.org/10.1029/94JB03097

Nettles, M., & Dziewoński, A. M. (2008). Radially anisotropic shear velocity structure of the upper mantle globally and beneath North America. *Journal of Geophysical Research*, *113*, B02303. https://doi.org/10.1029/2006JB004819

O'Driscoll, L. J., & Miller, M. S. (2015). Lithospheric discontinuity structure in Alaska, thickness variations determined by Sp receiver functions. *Tectonics*, *34*, 694–714. https://doi.org/10.1002/2014TC003669

Page, R. A., Stephens, C. D., & Lahr, J. C. (1989 Nov 10). Seismicity of the Wrangell and Aleutian Wadati-Benioff zones and the North American plate along the Trans-Alaska crustal transect, Chugach Mountains and Copper River basin, southern Alaska. *Journal of Geophysical Research*, *94*(B11), 16,059–16,082.

Pavlis, G. L., Bauer, M. A., Elliott, J. L., Koons, P., Pavlis, T. L., Ruppert, N., et al. (2019 Jan 29). A unified three-dimensional model of the lithospheric structure at the subduction corner in southeast Alaska: Summary results from STEEP. *Geosphere*, *15*(2), 382–406. https://doi.org/10.1130/GES01488.1

Perttu, A., Christensen, D., Abers, G., & Song, X. (2014). Insights into mantle structure and flow beneath Alaska based on a decade of observations of shear wave splitting. *Journal of Geophysical Research: Solid Earth*, *119*, 8366–8377. https://doi.org/10.1002/2014JB011359

Plafker, G., & Berg, H. C. (Eds) (1994). *The geology of Alaska*. Boulder, Colorado: Geological Society of America.editors

Ritzwoller, M. H., & Feng, L. (2019). Overview of pre- and post-processing of ambient noise correlations. In N. Nakata, L. Gualtieri, & A. Fichtner (Eds.), *Ambient seismic noise* (pp. 144–187). Cambridge: Cambridge University Press. https://doi.org/10.1017/9781108264808.007

Ritzwoller, M. H., Lin, F. C., & Shen, W. (2011). Ambient noise tomography with a large seismic array. *Comptes Rendus Geoscience*, *343*(8-9), 558–570. https://doi.org/10.1016/j.crte.2011.03.007

Rondenay, S., Montesi, L. G. J., & Abers, G. A. (2010). New geophysical insight into the origin of the Denali volcanic gap. *Geophysical Journal International*, *182*(2), 613–630. https://doi.org/10.1111/j.1365-246X.2010.04659.x

Shapiro, N. M., & Ritzwoller, M. H. (2002). Monte-Carlo inversion for a global shear velocity model of the crust and upper mantle. *Geophysical Journal International*, *151*(1), 88–105. https://doi.org/10.1046/j.1365-246X.2002.01742.x

Shapiro, N. M., Ritzwoller, M. H., Molnar, P., & Levin, V. (9 July 2004). Thinning and flow of Tibetan crust constrained by seismic anisotropy. *Science*, *305*(5681), 233–236. https://doi.org/10.1126/science.1098276

Shen, W., & Ritzwoller, M. H. (2016). Crustal and uppermost mantle structure beneath the United States. *Journal of Geophysical Research: Solid Earth*, *121*, 4306–4342. https://doi.org/10.1002/2016JB012887

Shen, W., Ritzwoller, M. H., Kang, D., Kim, Y., Lin, F., Ning, J., et al. (2016). A fast and reliable method for surface wave tomography. *A seismic reference model for the crust and uppermost mantle beneath China from surface wave dispersion*, *206*(2), 954–979. https://doi.org/10.1093/gji/ggw175

Shen, W., Ritzwoller, M. H., Schulte-Pelkum, V., & Lin, F.-C. (2013). Joint inversion of surface wave dispersion and receiver functions: A Bayesian Monte-Carlo approach. *Geophysical Journal International*, *192*, 807–836. https://doi.org/10.1093/gji/ggs050

Thomsen, L. (1986). Weak elastic anisotropy. *Geophysics*, *51*(10), 1954–1966. https://doi.org/10.1190/1.1442051

Tian, Y., & Zhao, D. (2012). Seismic anisotropy and heterogeneity in the Alaska subduction zone. *Geophysical Journal International*, *190*(1), 629–649. https://doi.org/10.1111/j.1365-246X.2012.05512.x

Venereau, C. M., Martin-Short, R., Bastow, I. D., Allen, R. M., & Kounoudis, R. (2019). The role of variable slab dip in driving mantle flow at the eastern edge of the Alaskan subduction margin: Insights from shear-wave splitting. *Geochemistry, Geophysics, Geosystems*, *20*, 2433–2448. https://doi.org/10.1029/2018GC008170

Wang, Y., & Tape, C. (2014). Seismic velocity structure and anisotropy of the Alaska subduction zone based on surface wave data. *Journal of Geophysical Research: Solid Earth*, *119*, 8845–8865. https://doi.org/10.1002/2014JB011438

Ward, K. M. (2015). Ambient noise tomography across the southern Alaskan Cordillera. *Geophysical Research Letters*, *42*, 3218–3227. https://doi.org/10.1002/2015GL063613

Ward, K. M., & Lin, F.-C. (2018). Lithospheric structure across the Alaska Cordillera from the joint inversion of surface waves and receiver functions. *Journal of Geophysical Research: Solid Earth*, *123*, 8780–8797. https://doi.org/10.1029/2018JB015967

Wech, A. G. (2016 Jul 1). Extending Alaska's plate boundary: Tectonic tremor generated by Yakutat subduction. *Geology*, *44*(7), 587–590. https://doi.org/10.1130/G37817.1

Wiemer, S., Tytgat, G., Wyss, M., & Duenkel, U. (1999). Evidence for shear-wave anisotropy in the mantle wedge beneath South Central Alaska. *Bulletin of the Seismological Society of America*, *89*(5), 1313–1322.

Xie, J., Ritzwoller, M. H., Brownlee, S., & Hacker, B. (2015). Inferring the oriented elastic tensor from surface wave observations: Preliminary application across the Western US. *Geophysical Journal International*, *201*(2), 996–1021. https://doi.org/10.1093/gji/ggv054

Xie, J., Ritzwoller, M. H., Shen, W., & Wang, W. (2017). Crustal anisotropy across Eastern Tibet and surroundings modeled as a depth-dependent tilted hexagonally symmetric medium. *Geophysical Journal International*, *209*, ggx004–ggx491. https://doi.org/10.1093/gji/ggx004

Xie, J., Ritzwoller, M. H., Shen, W., Yang, Y., Zheng, Y., & Zhou, L. (2013). Crustal radial anisotropy across Eastern Tibet and the Western Yangtze Craton. *Journal of Geophysical Research: Solid Earth*, *118*, 4226–4252. https://doi.org/10.1002/jgrb.50296

Yang, X., & Fischer, K. M. (1995). Seismic anisotropy beneath the Shumagin Islands segment of the Aleutian-Alaska subduction zone. *Journal of Geophysical Research*, *100*(B9), 18,165–18,177. https://doi.org/10.1029/95JB01425

Yang, X., & Gao, H. (2018). The cause and effect of slab segmentation in the Aleutian-Alaska subduction system. Abstract presented at 2018 AGU Fall Meeting, American Geophysical Union, Washington, DC.

Yuan, H. Y., Romanowicz, B., Fischer, K. M., & Abt, D. (2011). 3-D shear wave radially and azimuthally anisotropic velocity model of the North American upper mantle. *Geophysical Journal International*, *184*(3), 1237–1260. https://doi.org/10.1111/j.1365-246X.2010.04901.x

Zhang, Y., Li, A., & Hu, H. (2019). Crustal structure in Alaska from receiver function analysis. *Geophysical Research Letters*, *46*, 1284–1292. https://doi.org/10.1029/2018GL081011

Zhao, D., Christensen, D., & Pulpan, H. (1995). Tomographic imaging of the Alaska subduction zone. *Journal of Geophysical Research*, *100*(B4), 6487–6504. https://doi.org/10.1029/95JB00046